MNRAS 000, 1–22 (2019) Preprint 1 March 2019 Compiled using MNRAS LATEX style file v3.0

On the dust temperatures of high redshift galaxies

Lichen Liang[1]★, Robert Feldmann[1], Dušan Kereš[2], Nick Z. Scoville[3], Christopher C. Hayward[4], Claude-André Faucher-Giguère[5], Corentin Schreiber [6,7], Xiangcheng Ma[3,8], Philip F. Hopkins[3], Eliot Quataert[8]

[1]*Institute for Computational Science, University of Zurich, Zurich CH-8057, Switzerland*
[2]*Department of Physics, centre for Astrophysics and Space Sciences, University of California at San Diego, La Jolla, CA 92093, USA*
[3]*TAPIR, California Institute of Technology, Pasadena, CA, USA*
[4]*centre for Computational Astrophysics, Flatiron Institute, 162 Fifth Avenue, New York, NY 10010, USA*
[5]*Department of Physics and Astronomy and CIERA, Northwestern University, Evanston, IL 60208, USA*
[6]*Astrophysics, University of Oxford, Denys Wilkinson Building, Keble Road, Oxford OX1 3RH, United Kingdom*
[7]*Leiden Observatory, Leiden University, NL-2300 RA Leiden, The Netherlands*
[8]*Department of Astronomy, 501 Campbell Hall, University of California, Berkeley, CA, 94720, USA*

Accepted 2019. Received 2019; in original form 2019

ABSTRACT

Dust temperature is an important property of the interstellar medium (ISM) of galaxies. It is required when converting (sub)millimeter broadband flux to total infrared luminosity ($L_{\rm IR}$), and hence star formation rate, in high-z galaxies. However, different definitions of dust temperatures have been used in the literature, leading to different physical interpretations of how ISM conditions change with, *e.g.*, redshift and star formation rate. In this paper, we analyze the dust temperatures of massive ($M_{\rm star} > 10^{10}\,M_{\odot}$) $z = 2-6$ galaxies with the help of high-resolution cosmological simulations from the *Feedback in Realistic Environments* (FIRE) project. At $z \sim 2$, our simulations successfully predict dust temperatures in good agreement with observations. We find that dust temperatures based on the peak emission wavelength increase with redshift, in line with the higher star formation activity at higher redshift, and are strongly correlated with the specific star formation rate. In contrast, the *mass-weighted* dust temperature does not strongly evolve with redshift over $z = 2-6$ at fixed IR luminosity but is tightly correlated with $L_{\rm IR}$ at fixed z. The mass-weighted temperature is important for accurately estimating the total dust mass. We also analyze an 'equivalent' dust temperature for converting (sub)millimeter flux density to total IR luminosity, and provide a fitting formula as a function of redshift and dust-to-gas ratio. We find that galaxies of higher equivalent (or higher peak) dust temperature ('warmer dust') do not necessarily have higher mass-weighted temperatures. A 'two-phase' picture for interstellar dust can explain the different scaling relations of the various dust temperatures.

Key words: galaxies: evolution — galaxies: high-redshift — galaxies: ISM — submillimetre: galaxies

1 INTRODUCTION

Astrophysical dust, originating from the condensation of metals in stellar ejecta, is pervasive in the interstellar medium (ISM) of galaxies in both local and distant Universe (see *e.g.* Lagache et al. 1998; Riechers et al. 2010; Capak et al. 2011; Lombardi et al. 2014; Capak et al. 2015; Watson et al. 2015; Knudsen et al. 2016; Laporte et al. 2017; Harrington et al. 2017; Hashimoto et al. 2018, and references therein). Dust scatters and absorbs UV-to-optical light, and therefore strongly impacts the observed flux densities as well as the detectability of galaxies at these wavelengths (*e.g.* Calzetti et al. 1994; Kinney et al. 1993; Calzetti et al. 2000; Kriek & Conroy 2013; Narayanan et al. 2018). Despite that it accounts for no more than a few percent of the total ISM mass (Draine et al. 2007), dust also plays key role in a variety of physical and chemical processes associated with star formation and feedback processes in galaxies (*e.g.* Gould & Salpeter 1963; Cazaux & Tielens 2002; Murray et al. 2005; Murray et al. 2011; Hopkins et al. 2012; Zhang & Thompson 2012; Thompson et al. 2015; Crocker et al. 2018). Constraining and understanding dust properties of galaxies is therefore essential for proper interpretation of the multi-wavelength data from observations and for facilitating our understanding of galaxy formation and evolution.

Much of the stellar emission of star-forming galaxies is ab-

★ lliang@physik.uzh.ch

sorbed by dust grains and re-emitted at infrared-to-millimeter (mm) wavelengths as thermal radiation, encoding important information about dust and ISM properties (*e.g.* Madau & Dickinson 2014; Dunlop et al. 2016).

The advent of the new facilities in the past two decades, such as the *Spitzer Space Telescope* (Fazio et al. 2004), *Herschel Space Observatory* (Pilbratt et al. 2010), the Submillimetre Common-user Bolometer Array (SCUBA) camera on the James Clerk Maxwell Telescope (JCMT) (Holland et al. 1999, 2013), the AzTEC millimeter camera on the Large Millimeter Telescope (LMT) (Wilson et al. 2008), and the Atacama Large Millimeter/sub-millimeter Array (ALMA) has triggered significant interests in the study of ISM dust. In particular, observations with the Photodetector Array Camera and Spectrometer (PACS, Poglitsch et al. 2010) and the Spectral and Photometric Imaging Receiver (SPIRE, Griffin et al. 2010) instruments aboard *Herschel* made it possible to study the $70-500$ μm wavelength range where most of the Universe's obscured radiation emerges, and many dust-enshrouded, previously unreported objects at distant space have been uncovered through the wide-area extra-galactic surveys (Eales et al. 2010; Lutz et al. 2011; Oliver et al. 2012). Far-infrared (FIR)-to-mm SED modelling of dust emission has therefore become possible for objects at high redshift ($z \sim 4$, Gruppioni et al. 2013; Schreiber et al. 2018) and basic physical properties such as dust mass, total IR luminosity[1] ($L_{\rm IR}$), star formation rate (SFR), and dust temperature can be extracted using SED fitting techniques (Walcher et al. 2010).

An often adopted approach is to fit the observed FIR-to-mm photometry by a single-temperature (T) modified blackbody (MBB) function (Hayward et al. 2011). The T parameter that yields the best-fit is then called the '*effective*' temperature of the galaxy. Another temperature also often adopted is the *'peak'* temperature, which is defined based on the emission peak assuming Wien's displacement law. The relation between the two depends on the form of fitting function (Casey 2012). While it is not obvious how these observationally-defined temperatures reflect the physical dust temperature of the galaxy, they are the most frequently adopted temperatures to analyze large statistical samples of data.

The scaling relations of dust temperature with other dust/galaxy properties, including the $L_{\rm IR}$-temperature and specific star formation rate (sSFR)-temperature relations, may be related to the physical conditions of the star-forming regions in distant galaxies and have attracted much attention (*e.g.* Magdis et al. 2012; Magnelli et al. 2012, 2014; Schreiber et al. 2018; Casey et al. 2018b). While observational studies define dust temperature in a variety of ways, they generally infer that the temperature increases with $L_{\rm IR}$ and sSFR of galaxies. An increase of dust temperature with redshift could explain the dearth of detected high-z ($z > 4$) sources among the recent surveys compared with expectation derived, for example, from the Meurer $z = 0$ IRX-β relation (Bouwens et al. 2016). The physical interpretation of these scaling relationships is not obvious, however, largely because it is unclear how different galaxy properties effect the shape of the dust SED, and hence the observationally-derived temperatures. Radiative transfer (RT) analyses of galaxy models are an important approach to overcome these challenges (*e.g.* Narayanan et al. 2010; Hayward et al. 2011, 2012; Hayward & Smith 2015; Narayanan et al. 2015; Safarzadeh et al. 2016; Camps et al. 2016; Trayford et al. 2017; Narayanan et al. 2017; Behrens et al. 2018; Liang et al. 2018; Privon et al. 2018; Narayanan et al. 2018, Ma et al. 2019).

Ground-based galaxy surveys at (sub)mm wavelengths (*e.g.* SCUBA, AzTEC and ALMA) are complementary to *Herschel* observations (*e.g.* Smail et al. 1997; Dunne et al. 2000; Geach et al. 2013; Umehata et al. 2015; Aravena et al. 2016; Dunlop et al. 2016; Walter et al. 2016; Hatsukade et al. 2016; Geach et al. 2017; Casey et al. 2018b; Franco et al. 2018a, and references therein). Deep (sub)mm surveys are capable of probing less actively star-forming (SFRs $\lesssim 100\,{\rm M}_\odot\,{\rm yr}^{-1}$) galaxies at $z \lesssim 4$ (*e.g.* Hatsukade et al. 2013; Chen et al. 2014; Ono et al. 2014; Zavala et al. 2018a). Furthermore, they are effective at uncovering sources at $z > 4$ due to the "negative-K correction" (*e.g.* Capak et al. 2015; Carniani et al. 2015; Fujimoto et al. 2016; Laporte et al. 2017; Casey et al. 2018b). However, deriving the total IR luminosities, and hence SFRs, of (sub)mm-selected sources without *Herschel* detected FIR counterparts, requires adopting a dust temperature (which we refer to as 'equivalent' temperature in this paper) and a functional shape for the dust SED (Bouwens et al. 2016; Casey et al. 2018b). Knowledge of the dust temperature is also essential to constrain the *obscured* cosmic star formation density beyond $z \sim 2$, where currently only reliable constraints from rest-frame UV measurements are available, via (sub)mm number counts derived from ALMA blind surveys (Casey et al. 2018a,b; Zavala et al. 2018b).

In this paper we study observationally-derived and the physical (mass-weighted) dust temperatures with the aid of high-resolution cosmological galaxy simulations. In particular, we study a sample of massive ($M_{\rm star} > 10^{10}$ $M_\odot$) $z = 2-6$ galaxies from the FIRE project[2] (Hopkins et al. 2014) with dust RT modelling. This sample contains galaxies with $L_{\rm IR}$ ranging over two orders of magnitude, from 10^{10} to 10^{12} $L_\odot$ and few dust-rich, ultra-luminous ($L_{\rm IR} \gtrsim 10^{12}$ $L_\odot$) galaxies at $z \sim 2$ that are candidates for both *Herschel*- and submm-detected objects. A lot of them have $L_{\rm IR} \sim$ a few $\times 10^{11}$ $L_\odot$, which is accessible by *Herschel* using stacking techniques (*e.g.* Thomson et al. 2017; Schreiber et al. 2018). Our sample also contains fainter galaxies at $z = 2-6$ with observed flux densities $S_{870\mu{\rm m}}$ ($S_{1.2{\rm mm}}$) $\gtrsim 0.1$ mJy, which could be potentially detected with ALMA. We calculate and explicitly compare their mass-weighted dust temperature with the observationally-derived temperatures, as well as their scaling relationships with several galaxy properties. We also provide the prediction for the *equivalent* temperature that is needed for deriving $L_{\rm IR}$ of galaxy from its observed single-band (sub)mm flux.

The paper is structured as follows. In Section 2, we introduce the simulation details and the methodology of radiative transfer modelling. In Section 3, we provide the various definitions of dust temperature, discuss the impact of dust-temperature on SED shape, and compare the specific predictions of our simulations with observations. In Section 4, we focus on the conversion from single-band (sub)mm broadband flux to $L_{\rm IR}$ and provide useful fitting formulae. In Section 5, we discuss the observational implications of our findings. We summarize and conclude in Section 6.

Throughout this paper, we adopt cosmological parameters in agreement with the nine-year data from the Wilkinson Microwave Anisotropy Probe (Hinshaw et al. 2013), specifically $\Omega_{\rm m} = 0.2821$, $\Omega_\Lambda = 0.7179$, and $H_0 = 69.7$ km s^{-1} Mpc^{-1}.

[1] In this paper, $L_{\rm IR}$ is defined as the luminosity density integrated over the 8-1000 μm wavelength interval.

[2] fire.northwestern.edu

2 SIMULATION METHODOLOGY

In this section, we introduce our simulation methodology. In Section 2.1, we briefly summarize the details of the cosmological hydrodynamic simulations from which our galaxy sample is extracted. In Section 2.2, we introduce the methodology of our dust RT analysis and present mock images produced with SKIRT.

2.1 Simulation suite and sample

We extract our galaxy sample from the MASSIVEFIRE cosmological zoom-in suite (Feldmann et al. 2016; Feldmann et al. 2017), which is part of the Feedback in Realistic Environments (FIRE) project.

The initial conditions for the MASSIVEFIRE suites are generated using the MUSIC code (Hahn & Abel 2011) within a $(100\ \mathrm{Mpc/h})^3$ comoving periodic box with the WMAP cosmology. From a low-resolution (LR) dark matter (DM)-only run, isolated halos were selected that have a variety of halo masses and environmental overdensities (measured within 1.8 Mpc from the halo centre). Initial conditions for the 'zoom-in' runs use a convex hull surrounding all particles within $3R_{\rm vir}$ at $z = 2$ of the chosen halo defining the Lagrangian high-resolution (HR) region. The mass resolution of the default HR runs are $m_{\rm DM} = 1.7 \times 10^5\ M_\odot$ and $m_{\rm gas} = 3.3 \times 10^4\ M_\odot$, respectively. The initial mass of the star particle is set to be the same as the parent gas particle from which it is spawned in the simulations.

The simulations are run with the gravity-hydrodynamics code GIZMO[3] (FIRE-1 version) in the Pressure-energy Smoothed Particle Hydrodynamics ("P-SPH") mode (Hopkins 2015), which improves the treatment of fluid mixing instabilities and includes various other improvements to the artificial viscosity, artificial conductivity, higher-order kernels, and time-stepping algorithm designed to reduce the most significant known discrepancies between SPH and grid methods (Hopkins 2012). Gas that is locally self-gravitating and has density over 5 cm^{-3} is assigned an SFR $\dot{\rho} = f_{\rm mol}\rho/t_{\rm ff}$, where $f_{\rm mol}$ is the self-shielding molecular mass fraction. The simulations explicitly incorporate several different stellar feedback channels (but not feedback from supermassive black holes) including 1) local and long-range momentum flux from radiative pressure, 2) energy, momentum, mass and metal injection from supernovae (Types Ia and II), 3) and stellar mass loss (both OB and AGB stars) and 4) photo-ionization and photo-electric heating processes. We refer the reader to Hopkins et al. (2014) for details.

In the present study we analyze 18 massive ($10^{10} < M_{\rm star} < 10^{11.3}\ M_\odot$ at $z = 2$) central galaxies (from Series A, B and C in Feldmann et al. 2017) and their most massive progenitors (MMP) up to $z = 6$, identified using the Amiga Halo Finder (Gill et al. 2004; Knollmann & Knebe 2009). These galaxies are extracted from halos residing in a variety of environmental over-densities and accretion history. In order to better probe the dusty, IR-luminous galaxies at the extremely high-redshift ($z > 4$) Universe, we also include another 11 massive ($10^{10} < M_{\rm star} < 10^{11}\ M_\odot$ at $z = 6$) galaxies extracted from a different set of MASSIVEFIRE simulations that stop at $z = 6$, which are presented here for the first time. The latter were run with the same physics, numerics, and spatial and mass resolution, but were extracted from larger simulation boxes (400 Mpc/h and 762 Mpc/h on a side, respectively).

[3] A public version of GIZMO is available at http://www.tapir.caltech.edu/phopkins/Site/GIZMO.html

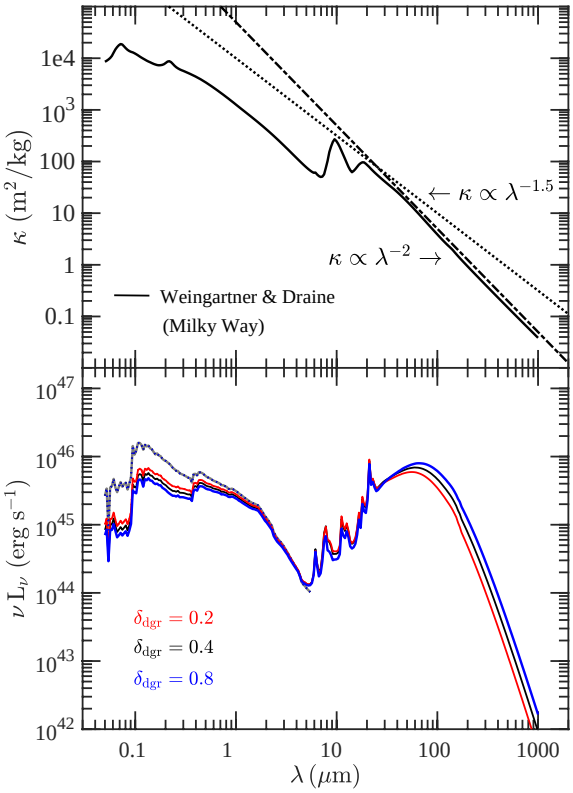

Figure 1. *Upper panel:* The dust opacity curve for the dust model used in this paper. The dashed and dash-dotted lines show the asymptotic power law $\kappa \propto \lambda^{-1.5}$ and $\kappa \propto \lambda^{-2.0}$, respectively. *Lower panel:* The SEDs of a selected $z = 2$ MASSIVEFIRE galaxy. The red, black and blue curves show results for $\delta_{\rm dzr} = 0.2$, 0.4 and 0.8, respectively. The grey curve shows the intrinsic stellar emission. About half of the stellar radiative energy of this galaxy is absorbed and re-emits at IR.

FIRE simulations successfully reproduce a variety of observed galaxy properties relevant for the present work, such as the stellar-to-halo-mass relation (Hopkins et al. 2014; Feldmann et al. 2017), the sSFRs of galaxies at the cosmic noon ($z \sim 2$) (Hopkins et al. 2014; Feldmann et al. 2016), the stellar mass – metallicity relation (Ma et al. 2015), and the sub-mm flux densities at 850 μm (Liang et al. 2018).

2.2 Predicting dust SED with SKIRT

We generate the UV-to-mm spectral energy distribution (SED) using the open source[4] 3D dust Monte Carlo RT code SKIRT (Baes et al. 2011; Baes & Camps 2015). SKIRT accounts for absorption and anisotropic scattering of dust and self-consistently calculates the dust temperature. We follow the approach by Camps et al. (2016) (see also Trayford et al. 2017) to prepare our galaxy snapshots as RT input models.

Each star particle in the simulation is treated as a 'single stellar population' (SSP). The spectrum of a star particle in the simulation is assigned using STARBURST99 SED libraries. In our default RT model, every star particle is assigned an SED according to the age and metallicity of the particle.

[4] SKIRT code repository: https://github.com/skirt

While our simulations have better resolution than many previous simulations modeling infrared and sub-mm emission (e.g., Narayanan et al. 2010; Hayward et al. 2011; De Looze et al. 2014) and can directly incorporate various important stellar feedback processes, they are still unable to resolve the emission from HII and photo-dissociation regions (PDR) from some of the more compact birth-clouds surrounding star-forming cores. The time-average spatial scale of these HII+PDR regions typically vary from $\sim$ 5 pc to $\sim$ 800 pc depending on the local physical conditions (Jonsson et al. 2010). Hence, in our alternative RT model, star particles are split into two sets based on their age. Star particles formed less than 10 Myrs ago are identified as 'young star-forming' particles, while older star particles are treated as above. We follow Camps et al. (2016) in assigning a source SED from the MAPPINGSIII (Groves et al. 2008) family to young star-forming particles to account for the pre-processing of radiation by birth-clouds. Dust associated with the birth-clouds is removed from the neighbouring gas particles to avoid double-counting.

We present in Section 3 and 4 the results from our default ('no birth-cloud') model. In Section 5 we will show that none of our results are qualitatively altered if we adopt the alternative RT model and account for unresolved birth-clouds.

Our RT analysis uses 10^6 photon packets for each stage. We use an octree for the dust grid and keep subdividing grid cells until the cell contains less than $f = 3 \times 10^{-6}$ of the total dust mass and the V-band optical depth in each cell is less than unity. The highest grid level corresponds to a cell width of $\sim$ 20 pc, *i.e.*, about twice the minimal SPH smoothing length. For all the analysis in this paper, we adopt the Weingartner & Draine (2001) dust model with Milky-Way size distribution for the case of $R_V = 3.1$. At FIR, the dust opacity can be well described by a power law, $\kappa_\lambda \propto 0.05\,(\lambda/870\mu\mathrm{m})^{-\beta}\,\mathrm{m}^2/\mathrm{kg}$, where $\beta \approx 2.0$ (see the *upper panel* of Figure 1) is the dust emissivity spectral index (consistent with the observational constraints, *e.g.* Dunne et al. 2000; Draine et al. 2007). Gas hotter than 10^6 K is assumed to be dust-free due to sputtering (Hirashita et al. 2015). We self-consistently calculate the self-absorption of dust emission by dust and include the transient heating function to calculate non-local thermal equilibrium (NLTE) dust emission by transiently heated small grains and PAH molecules (Baes et al. 2011). Transient heating influences the rest-frame MIR emission ($\lesssim$80 μm) but has minor impact on the FIR and (sub)mm emission (Behrens et al. 2018). SKIRT outputs $T_{\rm mw}$ for each cell that is obtained by averaging the temperature over grains of different species (composition and size). A galaxy-wide dust temperature is calculated by mass-weighting $T_{\rm mw}$ of each cell in the galaxies. At high redshift ($z > 4$), the radiation field from the cosmic microwave background (CMB) starts to affect the temperature of the cold ISM. We account for the CMB by adopting a corrected dust temperature (da Cunha et al. 2013)

$$T_{\rm dust}^{\rm corr}(z) = \left[T_{\rm dust}^{4+\beta} + T_{\rm CMB}^{4+\beta}(z) - T_{\rm CMB}^{4+\beta}(z=0)\right]^{1/(4+\beta)}, \quad (1)$$

where $T_{\rm CMB}(z) = 2.73\,(1+z)$ K is the CMB temperature at z.

For this study, we assume that dust mass traces metal mass in the ISM, and adopt a constant dust-to-metal mass ratio $\delta_{\rm dzr} = 0.4$ (Dwek 1998; Draine et al. 2007) for our *fiducial* analysis. We also try two different cases where $\delta_{\rm dzr} = 0.2$ and $\delta_{\rm dzr} = 0.8$, and throughout the paper, we refer to these two *dust-poor* and *dust-rich* cases, respectively. In the lower panel of Figure 1, we show the galaxy SED for the three models. $L_{\rm IR}$ increases when $\delta_{\rm dzr}$ increases because a higher optical depth leads to more absorption of stellar light and more re-emission at IR.

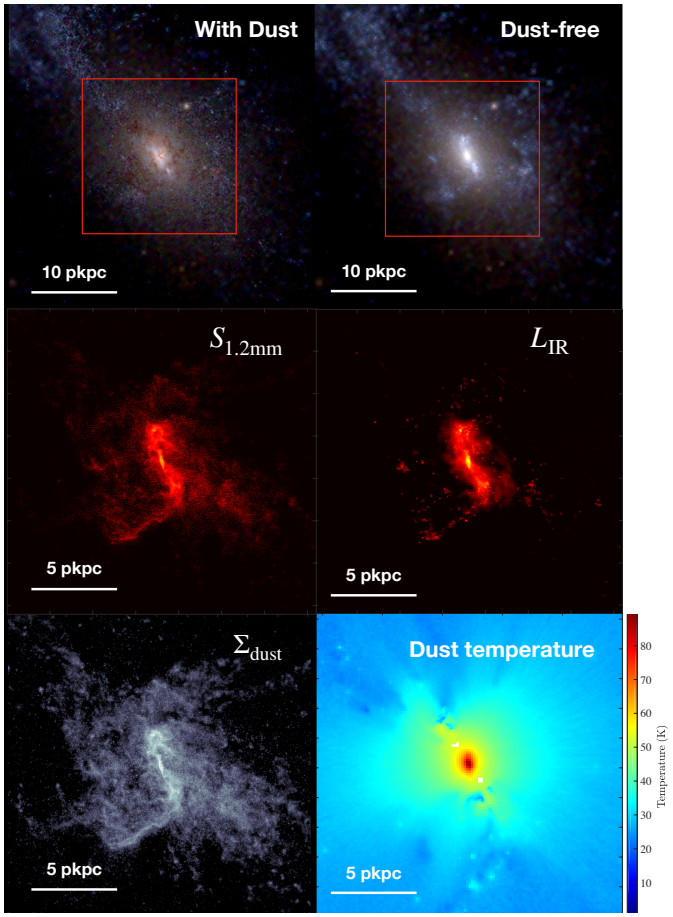

Figure 2. Example of the radiative transfer analysis applied to a $z = 2$ MASSIVEFIRE galaxy. *Upper panels*: UVJ image with (left) and without (right) the effect of dust extinction. *Middle panels*: The normalized $S_{1.2\rm mm}$ (left) and normalized $L_{\rm IR}$ (right). Compared with , $L_{\rm IR}$ traces more tightly to the star-forming regions. *Lower panels*: The dust surface density (left) and the dust temperature weighted along the line-of-sight, weighted by mass (right). The middle and lower panels show the result for the zoomed-in region enclosed by the red box in the upper panels.

SKIRT produces spatially resolved, multi-wavelength rest-frame SEDs for each galaxy snapshot observed from multiple viewing angles. For the analysis in this paper, SEDs are calculated on an equally spaced logarithmic wavelength grid ranging from rest-frame 0.005 to 1000 μm. We convolve the simulated SED output from SKIRT with the transmission functions of the PACS (70, 100, 160 μm), SPIRE (250, 350, 500 μm), SCUBA-2 (450, 850 μm), ALMA band 6 (870 μm) and 7 (1.2 mm) to yield the broadband flux density for each band.

We show in Figure 2 the result of running SKIRT on one of our galaxies. In particular we show a compositive U, V, J false-color image with and without accounting for dust absorption, scattering, and emission. We also show the image of ALMA 1.2 mm flux density, total IR luminosity, dust surface density and temperature. It can be seen that the 1.2 mm flux density traces the dust mass distribution, while IR luminosity appears to be more localized to the high-temperature region, since it is expected to be sensitive to temperature ($L \sim MT^{4+\beta}$). The local radiative intensity, the dust temperatures, and the dust density all peak in the central region of the galaxy.

3 UNDERSTANDING DUST TEMPERATURE AND ITS SCALING RELATIONS

In this section, we study the various scaling relations of dust temperature and examine the physical origins of the different scaling relations using the MASSIVEFIRE galaxy sample. First, we review the different ways of defining galaxy dust temperature that have been used in different observational and theoretical studies (Section 3.1), and compute the different temperatures for the MASSIVEFIRE sample (Section 3.2). we compare the calculated dust temperature(s) of the simulated galaxies with recent observational data (Section 3.3). Finally, we reproduce several observed scaling relations (*e.g.* $L_{\rm IR}$ vs. temperature, sSFR vs. temperature) with the simulated galaxies and provide physical insights for these relations (Section 3.4).

3.1 Defining dust temperature

Dust temperature has been defined in different ways by observational and theoretical studies. Here, we focus on four different possibilities, which we call *mass-weighted*, *peak*, *effective*, and *equivalent* dust temperature.

Mass-weighted dust temperature $T_{\rm mw}$
$T_{\rm mw}$ is the physical, mass-weighted temperature of dust in the ISM. $T_{\rm mw}$ is often explicitly discussed in theoretical studies where dust radiative transfer modelling is applied to the snapshots from the galaxy simulations, and dust temperature is calculated using LTE (for large grains) and non-LTE (for small grains and PAH molecules) approaches (*e.g.* Behrens et al. 2018; Liang et al. 2018).

Peak dust temperature $T_{\rm peak}$
The peak dust temperature is defined based on the wavelength $\lambda_{\rm peak}$ at which the far-infrared spectral flux density reaches a maximum

$$T_{\rm peak} = \frac{2.90\times10^3\ \mu{\rm m}\cdot{\rm K}}{\lambda_{\rm peak}}. \quad (2)$$

The peak wavelength $\lambda_{\rm peak}$ is commonly derived from fitting the SED to a specific functional form, for instance, a modified black body (MBB), see below.

Effective dust temperature $T_{\rm eff}$
The effective temperature is obtained by fitting the SED with a parametrized function. The effective temperature is thus a fit parameter this depends not only on the adopted functional form but also on the broadband photometry used in the fit.

For most observed SEDs, the RJ side of the dust continuum can be well described by a generalized modified-blackbody function (**G-MBB**) of the form (Hildebrand 1983)

$$S_{\nu_0}(T) = A\,\frac{(1+z)}{d_{\rm L}^2}\left(1-e^{-\tau_\nu}\right)B_\nu(T) \quad (3)$$

$$= \frac{1-e^{-\tau_\nu}}{\tau_\nu}\,\frac{(1+z)}{d_{\rm L}^2}\,\kappa_\nu M_{\rm dust}\,B_\nu(T) \quad (4)$$

where $\nu_{\rm o}$ is the observer's frequency, $\nu = \nu_{\rm o}\,(1+z)$ is the rest-frame frequency, τ_ν is the dust optical depth at ν[5], κ_ν is the dust opacity (per unit dust mass) at ν, $B_\nu(T)$ is the Planck function, A is the surface area of the emitting source and $d_{\rm L}$ is the luminosity distance from the source. The Wien side of the dust emission is expected to be strongly affected by the warm dust component in the vicinity of the star-forming regions, which can significantly boost the luminosity of galaxy with only a small mass fraction, knowing $L \sim MT^{4+\beta}$. Observations also show a variety of SED shape at MIR (*e.g.* Kirkpatrick et al. 2012; Symeonidis et al. 2013). To better account for the emission at MIR, Casey (2012, hereafter C12) introduced a simple (truncated) power-law component to Eq. 3, giving rise to a G-MBB with an additional power-law component (**GP-MBB**)

$$S_{\nu_0}(T) = A\,\frac{(1+z)}{d_{\rm L}^2}\left[\left(1-e^{-\tau_\nu}\right)B_\nu(T) + N_{\rm pl}\,\nu^{-\alpha}e^{-(\nu_{\rm c}(T)/\nu)^2}\right]. \quad (5)$$

The dust optical depth τ_ν is often fitted by a power law at FIR wavelengths, *i.e.* $\tau_\nu = (\nu/\nu_1)^\beta$, where β is the spectral emissivity index and ν_1 is the frequency where optical depth is unity. Observational evidence has shown that the value of ν_1 varies system by system (Gonzalez-Alfonso et al. 2004). In principle, ν_1 can be determined from SED fitting given full FIR-to-mm coverage (C12). However, in practice, it is often taken to be a constant, ~1.5-3 THz (*i.e.* $\lambda_1 = c\,\nu_1^{-1} = 100-200\ \mu$m) (*e.g.* Zavala et al. 2018a; Casey et al. 2018a,b).

In the equation above, $N_{\rm pl}$ is the normalization factor, α is the power-law index, and $\nu_{\rm c}$ is a cutoff frequency where the power-law term turns over and no longer dominates the emission at MIR. We allow $N_{\rm pl}$ as a free parameter, fix $\alpha = 2.5$, and adopt the functional form of $\nu_{\rm c}(T)$ provided by C12. The latter were constrained by fitting the observational data of a sample of local IR-luminous galaxies from the Great-Origins All Sky LIRG Survey (GOALS, Armus et al. 2009).

In the optically-thin regime ($\tau \ll 1$), Eq.5 reduces to the optically-thin modified black body function (**OT-MBB**), (see *e.g.* Hayward et al. 2011)

$$\begin{aligned} S_{\nu_0} &= \frac{(1+z)}{d_{\rm L}^2}\kappa_\nu M_{\rm dust}B_\nu(T) \\ &= \frac{(1+z)}{d_{\rm L}^2}\kappa_{870}\left(\frac{\nu}{\nu_{870}}\right)^\beta M_{\rm dust}B_\nu(T) \\ &= C_\nu(z)M_{\rm dust}B_\nu(T) \end{aligned} \quad (6)$$

where κ_{870} is the opacity at 870 μm ($\kappa_{870} = 0.05\,{\rm m^2\,kg^{-1}}$ for the dust model used in this work), $\nu_{870} = 343$ GHz, and $C_\nu(z)$ is a known constant for a given ν, $d_{\rm L}$, κ_{870}, β, and z.

The long-wavelength ($\lambda \gtrsim 200\ \mu$m) RJ tail of the dust emission, where dust optical depth becomes low, can be well fit by the above equation. However, Eq. 6 is also frequently adopted to fit the *full* dust SED, including both the Wien and the RJ sides, especially by the studies in the pre-*Herschel* era, when not enough data is available to well cover both sides from the SED peak (Magnelli et al. 2012). The single-T parameter in Eq. 6 is then often referred to as the 'dust temperature' of the galaxy. However, an effective temperature derived this way should be primarily understood as a fitting parameter and may not correspond to a *physical* temperature. In particular, it differs in general from the mass-weighted temperature of dust in a galaxy.

Equivalent dust temperature $T_{\rm eqv}$
We define $T_{\rm eqv}$ as the temperature that reproduces the actual IR lu-

[5] Throughout this paper, all ν and λ with no subscript stand for rest-frame quantities, while those with "o" are the observed quantities.

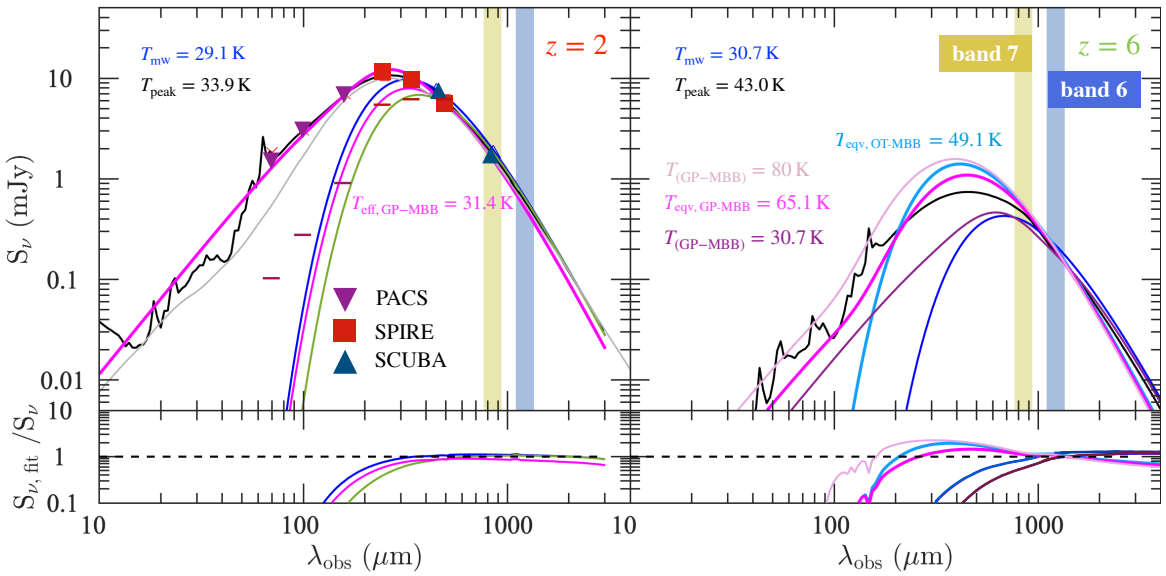

Figure 3. The SKIRT SED (black lines) of the selected $z = 2$ (*upper left panel*) and $z = 6$ (*upper right panel*) MASSIVEFIRE galaxies and the SED fitting functions (colored lines) for the two galaxies. In the *upper left panel*, the thick magenta line represents the GP-MBB function (Eq. 5, with $\alpha = 2.5$, $\beta = 2.0$ and $\lambda_1 = 100\mu$m) that best fits PACS + SPIRE + SCUBA + ALMA photometry calculated from its SKIRT SED. The thin magenta line represents the MBB component of the GP-MBB function. The derived effective temperature $T_{\rm eff}$ of the GP-MBB function is 31.4 K. The blue line shows the OT-MBB function (Eq. 6, with $\beta = 2.0$) with T being equal to the mass-weighted temperature $T_{\rm mw} = 29.1$ K of the galaxy. The green line shows the G-MBB function with the same $M_{\rm dust}$ and T but $\lambda_1 = 100\mu$m. **The optical depth in the G-MBB function results in a lower luminosity-to-mass ratio as well as a longer emission peak wavelength than the OT-MBB function with the same $M_{\rm dust}$ and T.** The calculated PACS, SPIRE and SCUBA flux densities of the galaxy are explicitly marked with the different symbols as labeled, and the horizontal ticks mark the confusion noise limit of the PACS/SPIRE bands. In the *upper right panel*, we show the GP-MBB (thick salmon, magenta and violet lines) and OT-MBB (light blue line) functions that are normalized to match the observed flux density at ALMA band 6 (1.2 mm). The magenta and light blue lines correspond to MBB functions with $T = T_{\rm eqv}$ that yield the correct $L_{\rm IR}$. The salmon (violet) line corresponds to GP-MBB function with $T > T_{\rm eqv}$ ($T < T_{\rm eqv}$) that leads to over(under)-estimate of $L_{\rm IR}$. Like in the upper left panel, we also show with blue line the OT-MBB function with $T = T_{\rm mw}$ and $M_{\rm dust}$ of the selected galaxy. In the two *upper panels*, the golden and grey shaded region mark ALMA band 7 and 6, respectively. In the *lower panels*, the colored lines show the ratio of the flux of the MBB fitting functions (excluding power-law component for the GP cases) to the simulated flux calculated by SKIRT that are shown in the *upper panels*. **An OT-MBB function with $T_{\rm mw}$ fits the RJ part of the dust SED quite well, while a GP-MBB function is able to also match the dust SED left of the peak.**

minosity for a given broadband flux (e.g., at 870 μm) and adopted parametrized functional form of the SED (e.g., OT-MBB). The value of $T_{\rm eqv}$ typically depends on both the observed frequency band as well as the SED form (Section 4).

In the specific case of optically-thin dust emission, the specific luminosity, can be written as

$$\begin{aligned} L_{\nu,\,\rm OT}(T, M_{\rm dust}) &= 4\pi(1+z)^{-1} d_{\rm L}^2 S_{\nu_{\rm o}} \\ &= 4\pi\kappa_\nu M_{\rm dust} B_\nu(T) \end{aligned} \tag{7}$$

By directly integrating the above formula over ν, one obtains the total IR luminosity (*e.g.* Hayward et al. 2011)

$$\begin{aligned} L_{\rm IR,\,OT}(T, M_{\rm dust}) &= \int_0^\infty 4\pi M_{\rm dust}\kappa_\nu B_\nu(T)\, d\nu \\ &= 4\pi M_{\rm dust}\kappa_{\nu_1}\nu_1^{-\beta}\left(\frac{k_B T}{h}\right)^{4+\beta}\left(\frac{2h}{c^2}\right) \\ &\quad \Gamma(4+\beta)\zeta(4+\beta) \\ &= \mathcal{D} M_{\rm dust} T^{(4+\beta)}, \end{aligned} \tag{8}$$

where $\mathcal{D}(\kappa_{\nu_1}, \nu_1, \beta)$ is a constant and Γ and ζ are Riemann functions.

Combining Eq. 8 and Eq. 6, $T_{\rm eqv}$ can now be defined as the temperature satisfying

$$L_{\rm IR}/S_{\nu_0} = \frac{\mathcal{D} T_{\rm eqv}^{4+\beta}}{C_\nu(z) B_\nu(T_{\rm eqv})}. \tag{9}$$

In the RJ regime, where $B_\nu(T_{\rm eqv}) = 2\nu^2 k_{\rm B} T_{\rm eqv}/c^2$,

$$L_{\rm IR}/S_{\nu_0} \propto T_{\rm eqv}^{3+\beta}. \tag{10}$$

$T_{\rm eqv}$ is therefore the temperature that one would need to adopt in order to obtain the correct IR luminosity and match the broadband flux density under the assumption that the SED has the shape of an OT-MBB function. Of course, the latter assumption is often a poor one and the actual SED shape can differ substantially from an OT-MBB curve. In this case, the equivalent temperature will be different from the mass-weighted dust temperature. Furthermore, the dust mass that is derived this way (via Eq. 6 for a given $T_{\rm eqv}$ and S_{ν_0}) will then differ from the actual physical dust mass.

In this paper we compute $T_{\rm eqv}$ based on Eq. 9 using the actual integrated IR luminosities and 870 μm (1.2 mm) flux densities unless explicitly noted otherwise. For equivalent temperatures based on G-MBB or GP-MBB spectral shapes, we numerically integrate Eq. 3 and Eq. 5 to obtain the IR luminosity for given a dust temperature and dust mass (analogous to Eq. 8 for the OT-MBB case).

3.2 The SEDs of simulated galaxies

In Figure 3 we show example SEDs of a $z = 2$ galaxy and a $z = 6$ galaxy from the MASSIVEFIRE sample. We separately discuss $z = 2$ and the $z = 6$ galaxies because the observational strategies for the two epochs are usually different. For $z = 2$, a IR-luminous (*i.e.* $L_{\rm IR} \gtrsim 10^{12}\, L_\odot$) galaxy may have both *Herschel*

coverage at FIR as well as (sub)mm coverage from ground-based facilities (*e.g.* SCUBA, ALMA and etc.). One can then *derive* the dust temperature ($T_{\rm peak}$ or $T_{\rm eff}$) from the observed FIR-to-mm photometry via SED fitting. In contrast, for galaxies at $z > 4$, most observations of the dust continuum cover only a single band (typically at ALMA band 6 or 7). Physical properties, such as $L_{\rm IR}$ and SFR, are thus often derived based on a single data point at (sub)mm, by *assuming* a dust temperature for the object. This approach is sensible if the adopted dust temperature is close to $T_{\rm eqv}$ of the given galaxy (see section 3.1).

3.2.1 *Example: The SED of a galaxy at $z = 2$*

For the $z = 2$ galaxy, we calculate the PACS (70, 100 and 160 μm) + SPIRE (250, 350 and 500 μm) + SCUBA-2 (450 and 850 μm) + ALMA (870 μm and 1.2 mm) broadband flux densities from the simulated SED. We fit its FIR-to-mm photometry — assuming successful detection at every band, as we show in the left panel that the PACS/SPIRE fluxes of this galaxy are above the confusion noise limit (marked by the horizontal ticks) (Nguyen et al. 2010; Magnelli et al. 2013) and the submm fluxes are above the typical sensitivity limit of SCUBA-2 and ALMA — by a GP-MBB function (with $\lambda_1 = 100$ μm, $\beta = 2.0$ and $\alpha = 2.5$) using least-χ^2 method. $N_{\rm pl}$ and T are left as two free parameters for the fitting. The best-fitting GP-MBB function is shown by the thick magenta line. The derived $T_{\rm eff}$ is 31.4 K, which is similar to its mass-weighted temperature ($T_{\rm mw} = 29.1$ K)[6]. From the best-fitting GP-MBB function (and also the simulated SED), $T_{\rm peak}$ is found to be 33.9 K.

For demonstration purpose, we also show with the blue line the exact solution of the OT-MBB function, with $T = T_{\rm mw} = 29.1$ K, $M_{\rm dust} = 5.4 \times 10^8\,M_\odot$, $\kappa_{870} = 0.05\,{\rm m^2\,kg^{-1}}$ and $\beta = 2.0$. As expected, the OT-MBB function with a mass-weighted temperature is in very good agreement with the galaxy SED at long wavelength. For this galaxy, at $\lambda = 100 - 650\,\mu$m ($\lambda_{\rm o} = 300\,\mu{\rm m} - 2\,{\rm mm}$), the difference between the flux of the OT-MBB function and the simulated flux is within 10% (illustrated by the lower left panel). At shorter wavelength, the emission is more tied to the dense, warm dust component in the galaxy, which is poorly accounted for by this OT-MBB function with a mass-weighted temperature. The OT-MBB function also appears to be slightly steeper than the simulated SED at longer wavelength, $\lambda_{\rm o} = 2$ mm, where the emission there is contributed more by the dust having a temperature lower than $T_{\rm mw}$. Overall, the OT-MBB function accounts for ~ 55% of $L_{\rm IR}$ of the galaxy, and the discrepancy is largely due to the MIR emission.

We also show the effect of optical depth. In the upper left panel, the green line shows the analytic solution from a G-MBB (Eq. 3) function with the same $M_{\rm dust}$ and T ($T = T_{\rm mw} = 29.1$ K), but with a power-law optical depth that equals unity at rest-frame $\nu_0 = 1.5$ THz, or $\lambda = 100\,\mu$m. While the emission looks identical to the optical-thin case (blue line) at long wavelength ($\lambda_{\rm o} > 500\,\mu$m), it appears to be lower at shorter wavelength when the effect of optical depth becomes important. The effect of optical depth is that the overall light-to-mass ratio is lower and the emission peak wavelength is longer than the optically-thin case.

[6] How well $T_{\rm eff}$ in the best-fitting GP-MBB function approximates $T_{\rm mw}$ depends on its parametrization (see Section 3.1). For instance, increasing λ_1 in Eq. 5 from 100 to 200 μm changes $T_{\rm eff}$ from 24.1 K to 48.2 K (see also Figure 20 of Casey et al. 2014).

3.2.2 *Example: The SED of a galaxy at $z = 6$*

Figure 3 also shows the SED of a $z = 6$ MASSIVEFIRE galaxy. This galaxy has lower $L_{\rm IR}$ ($3 \times 10^{11}\,L_\odot$) and $M_{\rm dust}$ ($8 \times 10^7\,M_\odot$) compared to the $z = 2$ galaxy, but interestingly, it has similar $T_{\rm mw}$ (30.7 K). The calculated flux densities at ALMA band 7 ($S_{870\,\mu{\rm m}}$) and 6 ($S_{1.2{\rm mm}}$) are 0.44 and 0.23 mJy, respectively. Like the $z = 2$ galaxy, an OT-MBB function (blue line) with $M_{\rm dust}$ and $T = T_{\rm mw}$ can well describe the emission of the $z = 6$ galaxy at long wavelength (for this case, $\lambda_{\rm o} > 1.2$ mm, or rest-frame $\lambda > 170\,\mu$m), but it only accounts for ~ 30% of $L_{\rm IR}$. A larger fraction of the total emission of this $z = 6$ galaxy origins from the warm dust component.

To estimate $L_{\rm IR}$ of a $z = 6$ galaxy from $S_{870\,\mu{\rm m}}$ (or $S_{1.2{\rm mm}}$), one often needs an assumed SED function and an assumed $T_{\rm eqv}$ for the adopted function. Since it is extremely difficult to constrain the details of SED shape at this high redshift, often a simple OT-MBB or GP-MBB function is used by the observational studies (*e.g.* Capak et al. 2015; Bouwens et al. 2016; Casey et al. 2018b). As an example, we fit the OT-MBB function to $S_{1.2{\rm mm}}$ of the $z = 6$ MASSIVEFIRE galaxy with varying T. We show in the right panel of Figure 3 the OT-MBB function (with fixed $\beta = 2.0$) that yields the simulated $L_{\rm IR}$ with the light blue line. The derived $T_{\rm eqv}$ for this function is 49.1 K. This is significantly higher than $T_{\rm mw}$, and as a result, the RJ side of the derived SED of this function appears to be much steeper than the simulated SED. It also poorly fits the simulated SED at wavelength close to $\lambda_{\rm peak}$. The derived $T_{\rm peak}$ is therefore very different from the true $T_{\rm peak}$ of the simulated SED.

We also fit $S_{1.2{\rm mm}}$ of this galaxy by a GP-MBB function ($\lambda_1 = 100\,\mu$m, $\beta = 2.0$, $\alpha = 2.5$). We show the result for $T = 30.7$ K (violet line), $T = 65.1$ (magenta line) and $T = 80$ K (salmon line). For $T = T_{\rm mw} = 30.7$ K, we use the same normalization of the power-law component as for the $z = 2$ galaxy (upper left panel), so that the SED shape is similar between these two galaxies. For $T = 65.1$ K and $T = 80.0$ K, we use the best-fitting normalization factor derived based on the local GOALS sample (see Table 1 of C12). We can see that the GP-MBB function appears to better describe the simulated SED shape compared with OT-MBB function, but in order to fit the simulated SED with reasonably good quality, a different choice of $N_{\rm pl}$ and λ_1 is needed. With $T = T_{\rm mw} = 30.7$ K, the GP-MBB function under-predicts the simulated $L_{\rm IR}$ ($3 \times 10^{11}\,L_\odot$) by 70%. Using $T_{\rm eqv,\,GP-MBB} = 65.1$ K, this function leads to the right $L_{\rm IR}$. We also show the result for $T = 80$ K, which over-predicts the $L_{\rm IR}$ by about a factor two.

In conclusion, we find that a OT-MBB function with a mass-weighted dust temperature well describe the long-wavelength ($\lambda \gtrsim 200\,\mu$m) part of the dust SED, but it does not well account for the Wien side of the SED and leads to significant under-estimate of $L_{\rm IR}$. A GP-MBB function can provide high-quality fitting to the simulated SED with good FIR+(sub)mm photometry of galaxy. Using single-band (sub)mm flux density of $z > 4$ galaxies, $T_{\rm eqv}$ is very different from $T_{\rm mw}$ of the galaxy. We will discuss $T_{\rm eqv}$ for high-z galaxies, its evolution with redshift and its dependence on other galaxy properties in more details in Section 4.

3.3 Comparing simulation to observation

Due to the high confusion noise level of the *Herschel* PACS/SPIRE cameras, most current observational studies on dust temperature at high-z are limited to the most IR-luminous galaxies in the Universe. For $z = 2$, the observations are generally limited to $L_{\rm IR} \gtrsim 10^{12}\,L_\odot$. Applying the powerful stacking technique to the *Herschel* images, it is also possible to probe the fainter regime of a few $10^{11}\,L_\odot$ at

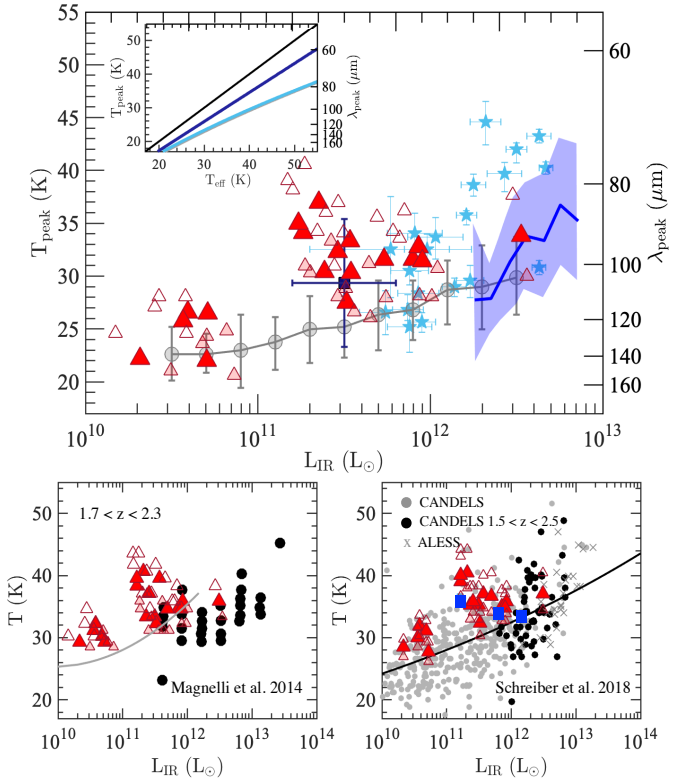

Figure 4. The dust temperature vs. $L_{\rm IR}$ relation of the $z \sim 2$ galaxies. The red triangles represent the simulated data of the MASSIVEFIRE sample at $z = 2$. The unfilled, filled, semi-transparent symbols show the result for the dust-poor ($\delta_{\rm dzr} = 0.2$), fiducial ($\delta_{\rm dzr} = 0.4$) and dust-rich ($\delta_{\rm dzr} = 0.8$) models, respectively. In the upper panel, we compare the simulated data to the observational results where dust temperature is derived using the SED fitting technique and with MBB-like functions (Eq. 3-6). The observation data by Zavala et al. (2018a) and the stacked result by Thomson et al. (2017) are represented by cyan asterisks and blue square, respectively. The blue shaded area shows 1-σ distribution of the compilation of high-z COSMOS galaxies by Lee et al. (2013). The grey circles and error bars show the binned result and its 1-σ distribution of the *Herschel*-selected sample at lower redshift ($z = 0 \sim 1.2$) from Symeonidis et al. (2013). To make fair comparison, we convert $T_{\rm eff}$ presented in Symeonidis et al. (2013) (grey line), Thomson et al. (2017) (dark blue line) and Zavala et al. (2018a) (cyan line) to $T_{\rm peak}$, and the relation between $T_{\rm peak}$ and $T_{\rm eff}$ is shown in the sub-figure that is over-plotted onto the upper panel. In the *lower panels*, we show the observational data derived using empirical SED templates. The stacked result by Magnelli et al. (2014) and the data from Schreiber et al. (2018) are shown in the *left and right panels*, respectively. The solid grey line in the *lower left panel* represents a second-order polynomial fit to the data points of a lower-redshift bin ($0.2 < z < 0.5$). The solid black line in the *lower right panel* represents the derived scaling relation by Schreiber et al. (2018) using the combined HRS+CANDELS+ALESS samples from local to $z \sim 4$. The blue squares show the stacked results for the three luminosity bins at $z \sim 2$. The dust temperature in the *lower panels* is defined using the same method as in Magnelli et al. (2014) and Schreiber et al. (2018). **The dust temperature of the $z = 2$ MASSIVEFIRE sample is in good agreement with the observational data.**

$z \sim 2$ (*e.g.* Thomson et al. 2017; Schreiber et al. 2018). Yet another problem with the observational studies is the strong selection bias with flux-limited surveys, meaning that the selected galaxy sample is limited to increasing IR luminosity with redshift. It is therefore non-trivial to disentangle the dependence of dust temperature on redshift and that on other galaxy properties. Using simulated sample, we do not expect to have such problem.

We start here by comparing the result of the MASSIVEFIRE sample at $z = 2$ with the observational data from similar redshift. This is where the luminosity range of our simulated galaxies share the largest overlap with the current observational data. At higher redshift, the observations are biased to higher $L_{\rm IR}$. In the following section, we will explicitly discuss the redshift evolution of dust temperature with the MASSIVEFIRE sample.

We present the result in Figure 4. In the upper panel, we compare the simulations with the observational data of which the (originally *effective*) dust temperature is derived using SED fitting technique and with MBB functions (*i.e.* Eq. 3-6), while in the lower panels, we show examples where the dust temperature of both the simulated and observation data is derived using the SED template libraries. In order to make fair comparison among different observations and with the simulation data, we convert all different $T_{\rm eff}$ presented in the literature to $T_{\rm peak}$ in the upper panel. $T_{\rm peak}$ of the simulated galaxies are derived from the best-fitting GP-MBB function (Eq. 5, with $\lambda_1 = 100\,\mu$m, $\beta = 2.0$ and $\alpha = 2.5$) to the FIR-to-mm photometry.

In the upper panel, we show with the blue shaded block the data from the H-ATLAS survey (Lee et al. 2013), that encompasses the high-z ($1.5 < z < 2.0$) *Herschel*-selected galaxies in the COSMOS field. The height of the block represents 1-σ distribution. We also explicitly show the $z = 1.5 - 2.5$ objects from Zavala et al. (2018a) (cyan asterisks), which are selected at 450 and 850 μm from the deep SCUBA-2 Cosmology Legacy Survey (S2CLS; Geach et al. 2017) probing the Extended Groth Strip (EGS) field. And finally, we present the stacked result by Thomson et al. (2017) (blue square), which is based on a high-z ($\langle z \rangle = 2.23$) sample extracted from the High-redshift Emission Line Survey (HiZELS) (Sobral et al. 2013), comprising 578 and 172 H_α-selected star-forming galaxies in the COSMOS and UDS fields, respectively. And for purpose of reference, we show the binned data from Symeonidis et al. (2013) by grey filled circles and error bars, which encompasses a *Herschel*-selected sample at $0.1 < z < 2$ selected from the COSMOS, GOODS-North and South fields. We convert the *effective* dust temperature $T_{\rm eff}$ presented in Symeonidis et al. (2013), Thomson et al. (2017) and Zavala et al. (2018a) to $T_{\rm peak}$. The relation between $T_{\rm peak}$ and $T_{\rm eff}$ for the fitting functions that are used by the two studies are over-plotted onto the upper panel as a sub-figure. Thomson et al. (2017) adopt a OT-MBB function (Eq. 6) with fixed $\beta = 1.5$, while Symeonidis et al. (2013) (Zavala et al. (2018a)) use a G-MBB function (Eq. 3) with fixed $\beta = 1.5$ ($\beta = 1.6$) and $\lambda_1 = 100\,\mu$m. From the sub-figure, we can see that $T_{\rm eff}$ presented in the three studies is higher than $T_{\rm peak}$.

In the lower panels, we compare the simulated result with the observational data from Magnelli et al. (2014) (left, hereafter M14) and Schreiber et al. (2018) (right, hereafter S18), both of which fit the galaxy photometry to the empirical SED template libraries. In particular, Magnelli et al. (2014) adopt the Dale & Helou (2002, hereafter DH02) SED template library and determine the temperature for each template by fitting their PACS+SPIRE flux densities with an OT-MBB function with fixed $\beta = 2.0$ and then finding the $T_{\rm eff}$ for the best-fitting OT-MBB function. Their sample comprises of *Herschel*-selected galaxies in GOODS-North, GOODS-South and COSMOS fields with reliable SFR, $M_{\rm star}$ and redshift estimates. The galaxies are binned in the SFR-$M_{\rm star}$-z plane and dust temperatures are inferred using the stacked FIR (100-500 μm) flux densities of the SFR-$M_{\rm star}$-z bins with least-χ^2 method. We show the stacked result for their $1.7 < z < 2.3$ redshift bin with the black filled dots in the *lower left panel*. For purpose of reference,

we also show with the solid grey line the result of a lower-redshift bin ($0.2 < z < 0.5$) in the same panel.

In the *lower right panel*, we also compare the simulation to the observational data of S18, of which the galaxy catalogue is based on the CANDELS survey (Grogin et al. 2011; Koekemoer et al. 2011), a $z = 2-4$ galaxy sample from the ALESS program (Hodge et al. 2013), as well as the local *Herschel* Reference Survey (Boselli et al. 2010). The temperature is derived by fitting the PACS+SPIRE photometry to the S18 SED template library, which is constructed based on the Galliano et al. (2011) elementary templates with an assumed power-law radiative intensity distribution. The temperature assigned to each template SED is the mass-weighted value of each elementary Galliano et al. (2011) template being used. We show in the *lower right panel* the result for the CANDELS sample with the black and grey filled circles. The black circles explicitly represent the objects at $z = 1.5 - 2.5$. We also show with blue squares the result of the stacked SEDs for $z = 1.5 - 2.5$ derived based on the PACS/SPIRE photometry in the CANDELS sample. The result of the ALESS sample at higher redshift ($z = 2 - 4$) is shown with grey crosses. The black curve shows the scaling relation $T \propto 5.57 L_{\rm IR}^{0.0638}$ that is derived by S18 using the combination of the CANDELS, ALESS and HRS samples.

For the simulated $z = 2$ galaxies, we fit their PACS/SPIRE photometry to the M14 and S18 SED templates using least-χ^2 method and find the temperature associated with the best-fitting template SED as defined in the literature. In other words, the temperature of the MASSIVEFIRE galaxies is not the same in each of the three panels. Comparing the simulated with the observational data, we find an encouragingly good agreement over the common range of $L_{\rm IR}$, with either the observational data derived using SED fitting technique (upper panel), or using SED templates (lower panels). And part from that, $T_{\rm peak}$ of the simulated $z = 2$ galaxies appear to show no clear correlation with $L_{\rm IR}$ in all three panels, at least at $L_{\rm IR} \gtrsim 10^{11}\,L_\odot$. This is consistent with the recent finding by S18 that the mean dust temperature derived from the stacked SEDs of the three $L_{\rm IR}$ bins of their $z \sim 2$ sample shows almost no correlation over the range of $1.5{\times}10^{11} - 1.5{\times}10^{12}\,L_\odot$ (blue squares). *This suggests that high-redshift galaxies do not necessarily follow a single, fundamental $L_{\rm IR} - T$ scaling relation*, which is typically derived using flux-limited observational data across a range of redshift but without much overlap of $L_{\rm IR}$ among different redshift bins. Ma et al. 2019 also show that the $L_{\rm IR} - T$ relation evolves with redshift at $z > 5$ using a different suite of FIRE simulations.

The observational data shows nontrivial scatter, which is particularly clear in the upper and lower right panels. At $L_{\rm IR} \approx 3 \times 10^{12}\,L_\odot$, for instance, $T_{\rm peak}$ (upper panel) is observed to be as low as ~ 25 K and as high as ~ 45 K. One possible reason is the intrinsic scatter of $\delta_{\rm dzr}$. We show in Figure 4 the result for the dust-poor ($\delta_{\rm dzr} = 0.2$) and dust-rich ($\delta_{\rm dzr} = 0.8$) models in each panel. The former (latter) show ~ 3 K increase (decrease) of dust temperature(s) compared with the fiducial model ($\delta_{\rm dzr}$). This difference, however, still appears to be relatively smaller compared to the scatter of the observational data. A larger variance of $\delta_{\rm dzr}$ may lead to a larger scatter of temperature. Apart from that, another reason could be the variance of the conditions of the ISM structure on the unresolved scale (*e.g.* compactness and obscurity of the birth-clouds embedding the young stars) could also contribute to the scatter. We will discuss more about the impact of sub-grid models later in Section 5. And finally, given that the *Herschel* cameras have fairly high confusion noise level, and it is rare that one galaxy has full reliable detection at every PACS/SPIRE+SCUBA band, we suggest that both factors can cause nontrivial uncertainty of observational result. Future infrared space telescope (*e.g.* SPICA, Spinoglio et al. 2017; Egami et al. 2018) spanning similar wavelength range and with higher sensitivity may help improve the constraint near emission peak and hence the observationally-derived dust temperatures.

We also note that $z = 2$ MASSIVEFIRE galaxies appear to show higher dust temperature compared to the lower-redshift counterparts in the observed sample, with either the temperature derived using SED fitting (*upper panel*) technique and or SED templates (*lower panels*). Observationally, how dust temperature evolves at fixed $L_{\rm IR}$ (or $M_{\rm star}$) from $z = 0$ to $z = 2$ is still being debated (*e.g.* Hwang et al. 2010; Magdis et al. 2012; Magnelli et al. 2013; Lutz 2014; Magnelli et al. 2014; Béthermin et al. 2015; Kirkpatrick et al. 2017; Schreiber et al. 2018). Uncertainties can potentially arise from selection effects (surveys at certain wavelengths preferentially select galaxies of warmer/colder dust) (*e.g.* Magdis et al. 2010; Hayward et al. 2011) and inconsistency in derivation of dust temperature. The dust temperature of galaxies in this redshift regime ($z < 2$) is beyond the scope of this paper.

3.4 The role of dust temperature in scaling relationships

The scaling relationships of dust temperature against other dust/galaxy properties (such as total IR emission, sSFR and etc.) have been extensively studied in the past decade because of the significant boost of the number of detected high-z dusty star-forming galaxies by *Herschel*, SCUBA and ALMA. We now have statistically large sample for revealing and studying the various scaling relationships of dust temperature. Here in this section, we show the result of the MASSIVEFIRE sample at $z = 2 - 6$, discuss the physical interpretation of the scaling relations and specifically examine how each scaling relation differs by using different dust temperatures ($T_{\rm mw}$ vs. $T_{\rm peak}$).

3.4.1 $S \propto MT$ (optically-thin regime)

As mentioned above, the long-wavelength RJ tail can be well described by a single-T OT-MBB function. This is a direct consequence of the rapid power-law decline of the dust opacity with wavelength as well as the fact that the coldest dust dominates the mass budget. At very long wavelength, the flux is only linearly dependent on T in the RJ tail, and therefore the overall shape of the SED on the RJ side is largely set by the temperature of the mass-dominating cold dust. Hence, it has been proposed that the flux density originating from the optically-thin part of the RJ tail can be used as an efficient measure for estimating dust and gas mass (by assuming a dust-to-gas ratio) of massive high-z galaxies (*e.g.* Scoville et al. 2014, 2016). Given the high uncertainties of the traditional CO methods and their long observing time, this approach represents an important alternative strategy for gas estimate (Scoville et al. 2017; Liang et al. 2018).

The RJ approach benefits from the effect of "negative K-correction". Eq. 6 can be re-written as (*e.g.* Scoville et al. 2016)

$$\begin{aligned} S_{\nu_{\rm o}}(T) &= \frac{(1+z)}{d_{\rm L}^2} 2 k_{\rm B} \kappa_\nu (\nu/c)^2 \Gamma_{\rm RJ}(\nu_0, z, T) M_{\rm dust} T \\ &= \psi(z) \Gamma_{\rm RJ} M_{\rm dust} T \end{aligned} \tag{11}$$

where $\Gamma_{\rm RJ}$ is the RJ correction function that accounts for the departure of the Planck function from RJ approximate solution in the rest frame, and $\psi(z)$ has the unit of mJy $M_\odot^{-1}$ K^{-1}. For given $\nu_{\rm o}$, $\kappa_\nu(\nu/c)^2$ scales as $(1+z)^4$ ($\beta = 2.0$). On the other hand, $(1+z)\,d_{\rm L}^{-2}$

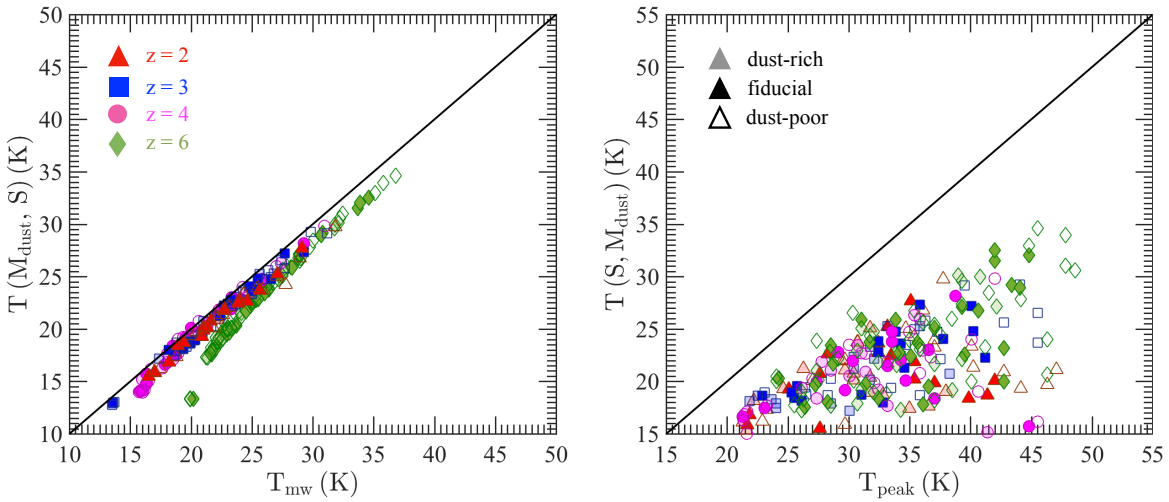

Figure 5. The relation of the temperature needed for dust mass estimate (calculated from Eq. 11) against $T_{\rm mw}$ (left panel) and $T_{\rm peak}$ (right panel) of the MASSIVEFIRE sample at $z = 2$ (red triangles), $z = 3$ (blue squares), $z = 4$ (magenta circles) and $z = 6$ (green diamonds). For the $z = 2-4$ galaxies, the flux density for mass estimate is measured at ALMA band 7 ($\lambda_{\rm o} = 870\,\mu$m), while for the $z = 6$ galaxies (green), it is measured at ALMA band 6 ($\lambda_{\rm o} = 1.2$ mm) so as ensure the rest-frame wavelength is on the optically-thin part of the RJ tail. The unfilled, filled and semi-transparent symbols represent the result for $\delta_{\rm dzr} = 0.2$, 0.4 and 0.8, respectively. The solid diagonal line marks the 1-to-1 locus. **$T_{\rm mw}$ is the temperature needed for estimating dust mass using the RJ-tail approach. $T_{\rm peak}$ is a poor proxy for this temperature.**

and $\Gamma_{\rm RJ}$ decline with redshift. The former term roughly scales as $(1+z)^{-2}$, while how $\Gamma_{\rm RJ}$ evolves with redshift depends on both $\nu_{\rm o}$ and T. The rise of $\kappa_\nu(\nu/c)^2$ with redshift can roughly cancel out or even reverse the decline of the other two components at $z \gtrsim 1$, with typical T of galaxies and (sub)mm bands. For example, with $T = 25$ K and ALMA band 6, $\psi\Gamma_{\rm RJ}$ stays about a constant from $z = 2-6$, while with ALMA band 7, $\psi\Gamma_{\rm RJ}$ declines *only* by less than a factor of two over the same redshift range (see Figure 2 of Scoville et al. 2016). (Sub)mm observations are therefore powerful for unveiling high-redshift dusty star-forming galaxies. In the RJ regime ($h\nu \ll k_{\rm B}T$), $\Gamma_{\rm RJ} \approx 1$ and S scales linearly to $M_{\rm dust}T$ at a given redshift.

The RJ approach relies on an assumed dust temperature. The proper temperature, T, needed for inferring dust (and gas) masses can be obtained from solving Eq. 11, given $S_{\nu_{\rm o}}$, $M_{\rm dust}$ and z. This required T value is close to the mass-weighted dust temperature, for galaxies from $z = 2$ to $z = 6$, and with varying $\delta_{\rm dzr}$, see Figure 5. The difference between these two temperatures is typically as small as 0.03 dex. This again confirms that a single-T OT-MBB function well describes the emission from the optically-thin RJ tail.

However, using $T_{\rm peak}$ will apparently lead to a poor constraint on $M_{\rm dust}$ and therefore gas mass of galaxy. First of all, it is systematically higher than $T_{\rm mw}$, and therefore can cause systematically underestimate of $M_{\rm dust}$. Secondly, there seems to be no strong correlation between $T_{\rm mw}$ and $T_{\rm peak}$ by comparing the *left* and *right panels*. So even by using $T_{\rm peak}$ to infer $T_{\rm mw}$ will produce systematic error. We will discuss the discrepancy between $T_{\rm peak}$ and $T_{\rm mw}$ in more details in the later sections. *Using other effective temperatures that have strong correlation with $T_{\rm peak}$ will be problematic as well.*

3.4.2 *The $L_{\rm IR}$ vs. $MT^{4+\beta}$ relation*

The scaling relation $L_{\rm IR} \propto M_{\rm dust}T^{(4+\beta)}$, which is frequently been adopted by many studies to probe and obtain useful physical insights for the star-forming conditions of the IR-luminous sources owing to its simplicity, is derived under the assumption of the optically-thin approximation (Eq. 8).

The temperature in the above scaling relation is a measure of the luminosity per unit dust mass and often viewed as a proxy for the internal radiative intensity. Yet, it is *not* obvious how this temperature parameter (*i.e.* $\sim (L_{\rm IR}/M_{\rm dust})^{1/6}$) is related to the physical, $T_{\rm mw}$ or the observationally accessible $T_{\rm peak}$.

We show in Figure 6 the scaling relation of the light-to-mass ratio, $L_{\rm IR}/M_{\rm dust}$ against $T_{\rm mw}$ (left panel) as well as $T_{\rm peak}$ (right panel) for the MASSIVEFIRE sample at $z = 2-6$, and we explicitly present the result for the fiducial (filled symbols), dust-poor (unfilled symbols) and dust-rich (semi-transparent symbols) cases.

In general, galaxy having higher dust temperature (both $T_{\rm mw}$ and $T_{\rm peak}$) emits more IR luminosity per unit dust mass. Focusing at first on $T_{\rm mw}$ (left panel), we see that $L_{\rm IR}/M_{\rm dust}$ of the MASSIVEFIRE galaxies appears to be systematically higher than from a simple single-T OT-MBB function (Eq. 7), which is indicated by solid black line in both panels. The offset (~ 0.3 dex) between the simulated result and the analytic solution is due to the higher emissivity of the dense, warm dust in vicinity of the star-forming regions (see lower panels of Figure 2), which accounts for a small fraction of the total dust mass but has strong emission, and shapes the Wien side of the overall SED of galaxy.

With all the galaxies from $z = 2$ to $z = 6$, we find that $L_{\rm IR}/M_{\rm dust}$ scales to $\approx T_{\rm mw}^{5.4}$. This is slightly flatter than the analytic solution derived using a single-temperature, optically-thin MBB function, *i.e.* $L_{\rm IR,\,OT}/M_{\rm dust} \propto T^6$ (Eq. 8). We understand the shallower slope as an optical depth effect. In the optically-thin regime ($\tau \ll 1$), $L/M \propto (1-e^{-\tau})/\tau \approx 1$, while in the optically-thick regime ($\tau \gg 1$), $L/M \propto \tau^{-1}$ (Eq. 4). In the optically-thick regime, $L_{\rm IR}/M_{\rm dust}$ therefore decreases with increasing τ. Galaxies of higher $T_{\rm mw}$ are more dust-rich (Section 3.4.3) and their star-forming regions tend to be more optically-thick, resulting in a flattening of the scaling relation.

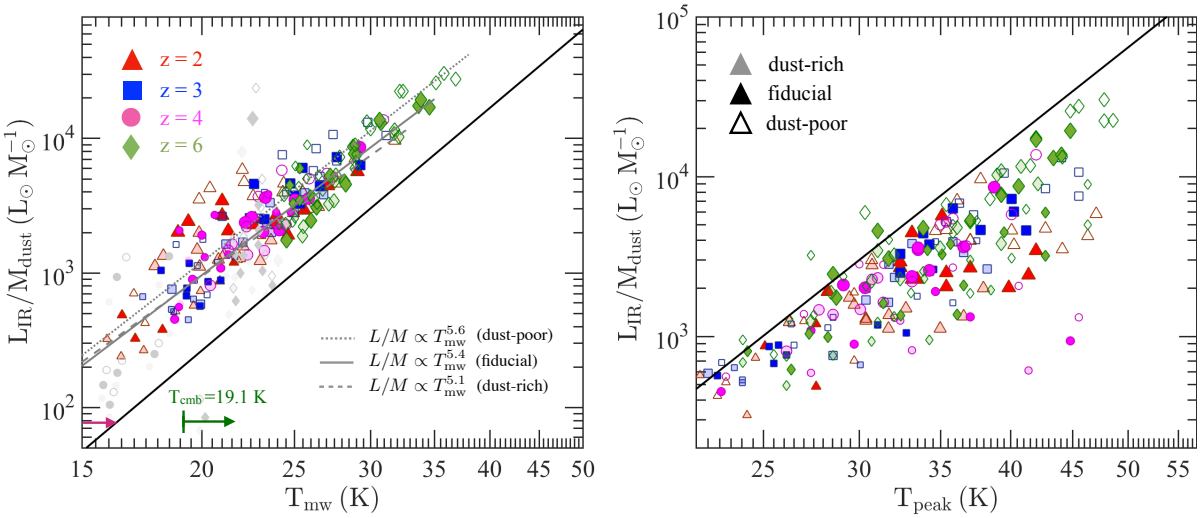

Figure 6. The relation of L_{IR}/M_{dust} against T_{mw} (*left panel*) and T_{peak} (*right panel*) of the MASSIVEFIRE sample at $z = 2-6$. The result for the fiducial, dust-poor and dust-rich cases are shown with unfilled, filled and semi-transparent symbols, respectively. We highlight the $z = 2$ and $z = 3$ galaxies having $L_{IR} \gtrsim 10^{11}$ $L_\odot$ by using larger-sized symbols. These are the objects currently detectable with stacking techniques (*e.g.* Thomson et al. 2017; Schreiber et al. 2018). In the left panel, the dotted, solid and dashed grey lines represent the best-fit power-law scaling relation for the dust-rich, fiducial and dust-poor cases, respectively. Those galaxies of which T_{mw} is strongly affected by CMB heating, *i.e.* $T_{mw} - T_{CMB}(z) < 5$ K, are coloured by grey. They are excluded from the power-law fitting. The dust-rich (poor) case exhibits a flatter (steeper) L_{IR}/M_{dust} vs. T_{mw} scaling relation compared with the fiducial model. The solid black line in each panel represents the expected analytic scaling using the optically-thin MBB function (Eq. 6), with the dust emissivity spectral index $\kappa_{870} = 0.05$ m^2 kg^{-1}.

Comparing the dust-poor (dust-rich) models with the fiducial case, T_{mw} on average is higher (lower) by $\sim$ 1.6 (0.9) K. This is due to the optical depth effect. By reducing the amount of dust, the chance of receiving a short-wavelength photon increases because the optical depth from the emitting sources decreases. Therefore, dust is expected to be heated to higher temperature to balance the increased amount of absorption. Apart from that, δ_{dzr} also mildly effects the normalisation of the L_{IR}/M_{dust} vs. T_{mw} relation. The dust-poor (dust-rich) case shows about 0.13 (0.06) dex higher (lower) L_{IR}/M_{dust}, on the average, than the fiducial case, indicating a high (lower) luminosity emitted per unit dust mass. This is because a larger (reduced) mass *fraction* of the total dust is heated by (can actually "see") the hard UV photons from the young stars due to the reduced optical depth (Scoville 2013; Scoville et al. 2016). This dust component can be efficiently heated to a temperature much higher than the mass-weighted average of the bulk (Harvey et al. 2013; Broekhoven-Fiene et al. 2018), and has a much higher L/M ratio than the rest.

T_{peak} (right panel) shows a much larger scatter than T_{mw}, and is less correlated with L_{IR}/M_{dust} than T_{mw}. It thus has lower power to predict the luminosity-to-dust-mass ratio. T_{peak} is also more affected by a change of δ_{dzr} as it is more sensitive to the mass *fraction* of ISM dust that is efficiently heated to high temperature by the hard UV photons emitted from young stars.

3.4.3 L_{IR} *vs. T relation*

The dust temperature vs. total IR luminosity is one most extensively studied scaling relations. We have shown in Section 3.2 that our simulations have successfully produced the result at $z = 2$ for galaxies that are in good agreement with the recent observational data at similar luminosity range. Here in this section, we focus on the evolution of dust temperature up to higher redshift. One major problem with the current observational studies on the $T-L$ scaling is the selection effects of the flux-limited FIR samples that have been used to probe such relation. Higher redshift sample is biased towards more luminous systems. How dust temperature evolves at fixed luminosity is still being routinely debated (see *e.g.* Magnelli et al. 2014; Béthermin et al. 2015; Casey et al. 2018b; Schreiber et al. 2018). We present the result using our sample with $L_{IR} \approx 10^9 - 2\times10^{12}$ $L_\odot$ from $z = 2-6$. For $z = 3-6$, there is no current data available that we can make direct comparison to at similar L_{IR} of our sample. Future generation of space infrared telescope, such as SPICA, can probe similar regime of IR luminosity at these epochs.

We present the temperature vs. luminosity relation of the MASSIVEFIRE galaxies at $z = 2-6$ in Figure 7. In the upper and lower left panels, we show T_{peak} vs. L_{IR} and T_{mw} vs. T_{IR} relation, respectively.

Focusing at first on T_{peak} vs. L_{IR} relation (*upper left*), we find a noticeable increase of T_{peak} with redshift at fixed L_{IR}, albeit with large scatter at each redshift. Looking at the most luminous galaxy at each redshift, we see that T_{peak} increases from about 34 K at $z = 2$ to $\sim$ 43 K at $z = 6$ for the fiducial dust model ($\delta_{dzr} = 0.4$). With all the luminous galaxies with $L_{IR} > 10^{11}$ $L_\odot$, we fit the evolution of T_{peak} with redshift as a power law and obtained

$$\log\left(\frac{T_{peak}(z)}{25\,\mathrm{K}}\right) = (-0.03 \pm 0.11) + (0.22 \pm 0.14)\log(1+z). \quad (12)$$

This result is in good quantitative agreement with the recent observational finding by Magnelli et al. (2014) and Schreiber et al. (2018).

For each redshift, there is also a mild trend of declining T_{peak} with decreasing L_{IR} over the three orders of magnitude of L_{IR} being considered. For instance, T_{peak} of the $z = 6$ galaxies at

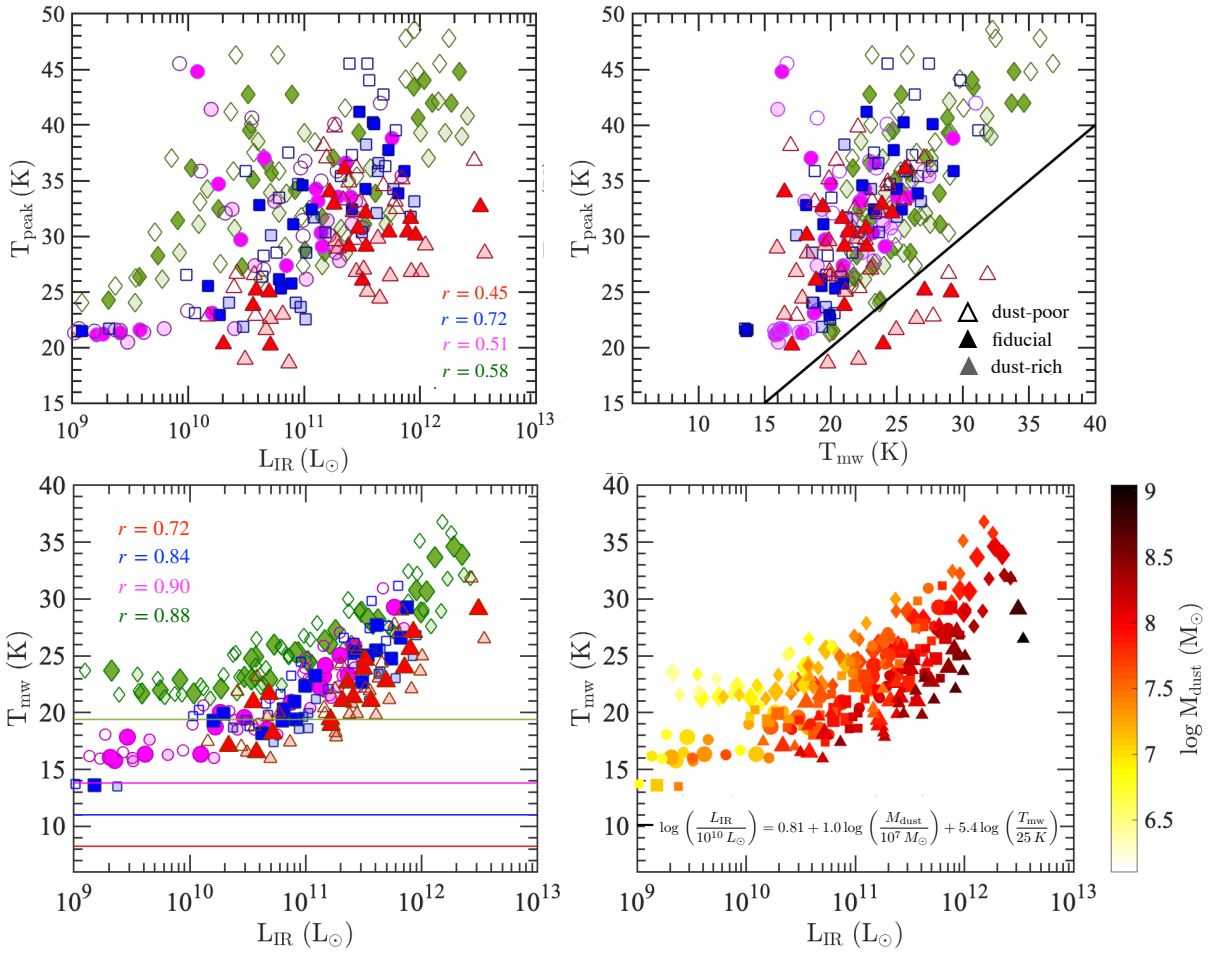

Figure 7. *Upper left*: T_{peak} vs. L_{IR} relation of the MASSIVEFIRE galaxies at $z = 2-6$. *Upper right*: The T_{peak} vs. T_{mw} relation. *Lower panels*: The T_{mw} vs. L_{IR} relation. In the *left panel*, galaxies are coloured by their redshift, while in the *right panel*, they are coloured by M_{dust}. The horizontal solid lines in the *lower left panel* represent the CMB temperature at each redshift. In the upper panels and the *lower left panel*, the filled, unfilled and the semi-transparent symbols represent the fiducial, dust-poor and dust-rich models, respectively. The data from all three dust models are included in the lower right panel.

$L_{IR} = 10^{10}\,L_\odot$ is about 32 K, which is about 10 K lower than the value at $L_{IR} = 10^{12}\,L_\odot$, and is similar to the value of the brightest objects at $z = 3$ and $z = 4$. We find some faint objects at $\sim 10^{10}\,L_\odot$ whose T_{peak} is as low as $\sim$ 20 K. We also note that the scatter of T_{peak} could be very large at the faint end even with the simple fiducial dust model. At $z = 4$, some objects could be as hot as $\sim$ 40 K, while some could be as cold as $\sim$ 20 K. This large scatter is mainly driven by the difference of sSFR among those galaxies, which we will discuss in more details in the following section.

With such large scatter, the correlation between T_{peak} and L_{IR} appears to be fairly weak. The Pearson correlation coefficient (r) of the T_{peak} vs. L_{IR} relation at individual redshift ranges from 0.45 to 0.72 at the redshifts being considered. For the $z = 2$ sample, there is no noticeable correlation at $L_{IR} > 10^{11}\,L_\odot$.

On the other hand, T_{mw} exhibits a tighter correlation with L_{IR} (lower left panel) (r ranging from 0.72 to 0.90), with an increase of the normalisation of the L_{IR}-T_{mw} relation with redshift. The increase of T_{mw} with redshift at fixed L_{IR} is clearly less prominent than T_{peak}. At $L_{IR} \approx 10^{12}\,L_\odot$, for example, T_{mw} increases from $\sim$ 27 K at $z = 2$ to only $\sim$ 32 K at $z = 6$. The CMB heating sets a temperature floor for T_{mw} at the low luminosity end.

The evolution of the T_{mw} vs. L_{IR} scaling is driven by M_{dust}. At fixed L_{IR}, galaxies at higher redshift have lower M_{dust}. This can be clearly seen from the *lower right panel*, where we colour the same data as in the *lower left panel* by M_{dust} of galaxy. There is clear sign of anti-correlation between T_{mw} and M_{dust} at fixed L_{IR} (see also Hayward et al. 2012; Safarzadeh et al. 2016; Kirkpatrick et al. 2017). Applying multi-variable linear regression analysis to the $z = 2-6$ galaxies, excluding those that are strongly affected by the heating of the CMB background (*i.e.* $T_{mw} \lesssim T_{CMB}(z) + 5$ K), we obtain the scaling relation

$$\log\left(\frac{L_{IR}}{10^{10}\,L_\odot}\right) = (0.81 \pm 0.07) + (1.01 \pm 0.06)\log\left(\frac{M_{dust}}{10^7\,M_\odot}\right) + (5.40 \pm 0.36)\log\left(\frac{T_{mw}}{25\,K}\right),$$
$$\text{or } L_{IR} \propto M_{dust}\,T_{mw}^{5.4}. \quad (13)$$

It appears to be shallower than the classical $L_{IR} \propto M_{dust} T^{(4+\beta)}$ relation derived based on the optically-thin approximation. We will discuss in Section 5 about using this scaling relation to estimate M_{dust} (or T_{mw}).

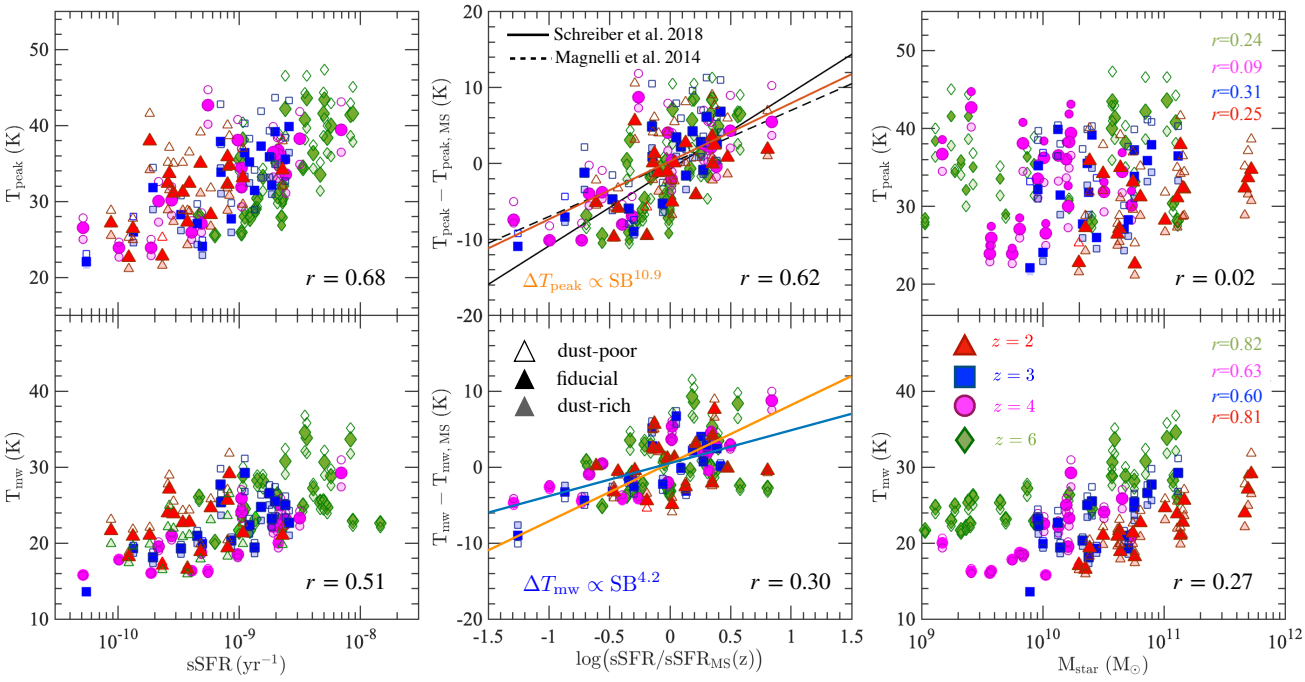

Figure 8. The relation of dust temperature against sSFR (left column), SB = sSFR/sSFR$_{\rm MS}(z)$ (middle column) and $M_{\rm star}$ (right column) of the MASSIVEFIRE galaxies at $z = 2$ (red triangles), $z = 3$ (blue squares), $z = 4$ (magenta circles) and $z = 6$ (green diamonds). We show the result with $T_{\rm peak}$ and $T_{\rm mw}$ in the upper and lower panels, respectively. The value of the Pearson correlation coefficient (r) for each relation is labeled in each panel. r is calculated using the galaxies with $T_{\rm mw}$ being sufficiently higher than the CMB temperature at given redshift, *i.e.* $T_{\rm mw} - T_{\rm CMB}(z) < 5$ K. The solid and dashed lines in the upper middle panel represent the observed scaling relation by Schreiber et al. (2018) and Magnelli et al. (2014), respectively. The orange and blue lines in the middle panels show the best-fitting line for the MASSIVEFIRE sample. The former and latter correspond to $T_{\rm peak}$ and $T_{\rm mw}$, respectively. $T_{\rm peak}$ **exhibits relatively stronger correlation with sSFR than $T_{\rm mw}$, but weaker correlation with $M_{\rm star}$.**

3.4.4 sSFR vs. T relation

The sSFR vs. dust temperature relation is one other frequently studied scaling relation which provide useful physical insights to dust temperature and is complementary to the $L_{\rm IR}$ vs. temperature relation.

In Figure 8, we show the relation of dust temperature against sSFR = SFR$_{\rm 20\,Myrs}/M_{\rm star}$ for the MASSIVEFIRE sample at $z = 2-6$ in the *left panels*. We present the result for $T_{\rm peak}$ and $T_{\rm mw}$ in the upper and lower *left panels*, respectively.

In general, dust temperature shows clear correlation with sSFR. Galaxies at higher redshift have, on average, higher sSFR, which is a direct consequence of the evolution of the star-formation main sequence. SFR is a proxy for the internal radiative intensity (most UV emission originates from the young stellar populations in the galaxies), and $M_{\rm dust}$ is about linearly scaled to $M_{\rm star}$ in the MASSIVEFIRE galaxies, the sSFR ($\sim$SFR/$M_{\rm dust}$) can be viewed as a proxy for the total energy input rate per unit dust mass. It is therefore expected that to first order, dust temperature is positively correlated with sSFR of galaxies. This is indeed what we can see from both of the *left panels* of Figure 8. For instance, the $z = 2$ galaxies (red) have a median sSFR of 3×10^{-9} $\rm yr^{-1}$ and median $T_{\rm mw} = 20$ K ($T_{\rm peak} = 30$ K). Both sSFR and dust temperature (both $T_{\rm peak}$ and $T_{\rm mw}$), on average, increases with redshift. The $z = 6$ sample (green) have a median sSFR of 2×10^{-8} $\rm yr^{-1}$ and median $T_{\rm mw} = 28$ K ($T_{\rm peak} = 37$ K).

The correlation persists when focusing on each individual redshift. In the middle panels, we show the result when both temperature and sSFR is normalised by the mean value of the whole sample (sSFR$_{\rm MS}$) at each different redshift. With $T_{\rm peak}$ (upper middle panel), the simulated galaxies, including all objects at $z = 2-6$, exhibit a strong correlation ($r = 0.62$) between starburstiness (*i.e.* SB = sSFR/sSFR$_{\rm MS}$(z)) and normalised $T_{\rm peak}$, and the derived scaling relation (solid orange line) is in qualitative agreement with the recent observations by Magnelli et al. (2014) (dotted black line) and Schreiber et al. (2018) (solid black line). We also find that compared to $L_{\rm IR}$, $T_{\rm peak}$ is more strongly correlated with sSFR at each given redshift, which is in agreement with the previous finding by Magnelli et al. (2014) (see also Lutz 2014).

However, due to the inhomogeneity of dust distribution in galaxies and the complexity in star-dust geometry, the radiative energy emitted from the young stellar populations is not expected to evenly heat the ISM dust in the galaxy. Most of the UV photons are absorbed by the dense dust cloud in vicinity of the young star-forming regions, while the majority of the dust in the ISM is heated by the old stellar populations with more extended distribution, as well as the secondary photons re-emitted from the dust cloud near the young star clusters. For such reason, $T_{\rm peak}$ is expected to be more sensitive to the emission from the warm dust component, which is more closely tied to the young star clusters, while $T_{\rm mw}$ is determined by the cold dust component and therefore can be relatively less sensitive to the sSFR of galaxy than $T_{\rm peak}$.

This indeed can be seen from comparing the *upper* and *lower middle panels* of Figure 8. First of all, $\Delta T_{\rm peak}$ ($T_{\rm peak} - T_{\rm peak,\,MS}$) shows a relatively stronger correlation with SB than $\Delta T_{\rm mw}$ ($T_{\rm mw} - T_{\rm mw,\,MS}$). With all the $z = 2-6$ MASSIVEFIRE galaxies, the Pearson correlation coefficient of the $\Delta T_{\rm peak}$ vs. SB scaling is $r = 0.62$,

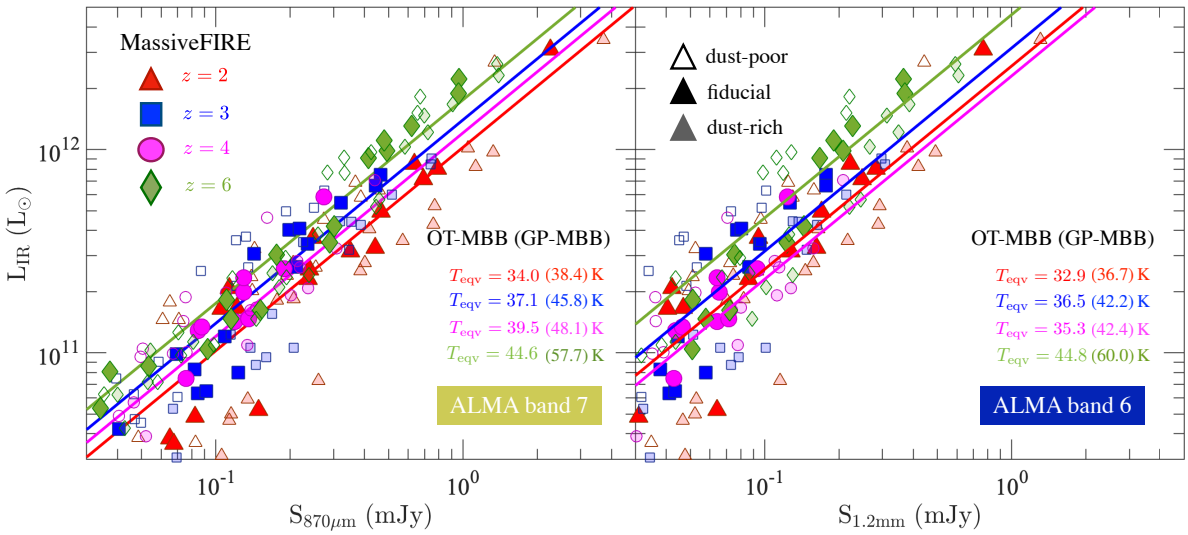

Figure 9. The relation of L_{IR} vs. $S_{870\mu m}$ (*left panel*) and $S_{1.2mm}$ (*right panel*) of our MASSIVEFIRE galaxy sample at $z = 2-6$. The unfilled, filled and semi-transparent symbols represent the result for a range of dust-to-metal ratios $\delta_{dzr} = 0.2$, $\delta_{dzr} = 0.4$ and $\delta_{dzr} = 0.8$, respectively. The coloured lines show the L_{IR} vs. $S_{870\mu m}$ (and $S_{1.2mm}$) relation expected from an OT-MBB function (Eq. 6, with fixed $\beta = 2.0$) with an equivalent temperature ($T_{eqv,\,OT-MBB}$) that yields the L_{IR} of the MASSIVEFIRE sample at each redshift. The sample-average value of T_{eqv} for each redshift, ALMA band, and SED fitting function is labeled in the figure. Overall, T_{eqv} increases with redshift for the galaxies in our sample.

while that of the ΔT_{mw} vs. SB scaling is $r = 0.30$. Secondly, over about two orders of magnitude of SB ($\sim 0.1 - 10$), the scaling relation with ΔT_{peak} appears to be relatively steeper,

$$\Delta T_{peak} \propto \mathrm{SB}^{\,10.93\pm2.57} \text{ vs. } \Delta T_{mw} \propto \mathrm{SB}^{\,4.21\pm0.98}. \quad (14)$$

This is because the UV photons from the young star clusters preferentially heat the dense dust cloud in the neighbourhood to high temperature, which boosts the MIR emission and helps shift the SED peak to shorter wavelength. However, the heating of the bulk of the dust is inefficient. The reason is that once the UV photons get absorbed and re-emit as FIR photons, the chance of them being absorbed by dust again becomes much lower as a consequence of the declining opacity with wavelength ($\kappa_\lambda \propto \lambda^{-2}$) (Scoville 2013). It is also interesting to note that both T_{peak} and T_{mw} are less correlated with SB when sSFR is averaged over longer period of time (Feldmann 2017). By averaging sSFR over a period of 100 Myrs instead of 20 Myrs, for example, r of the T_{peak} (T_{mw}) vs. SB relation declines from 0.62 (0.30) to 0.51 (0.23). Apart from that, the scaling relation of both temperatures becomes more flattened.

Finally, we show the relation between dust temperature against M_{star} in the *right panels*. Looking at the upper panel, it is clear that T_{peak} has very weak correlation with M_{star}. This again shows that T_{peak} is strongly influenced by the emission from the warm dust that is associated with the recently formed young stars and does not have as strong correlation with the total integrated star formation (or M_{star}) of a galaxy. In contrast, T_{mw} is less sensitive to the variance of recent star-forming conditions and therefore shows relatively small scatter at given M_{star} at each redshift. The normalisation of the T_{mw} vs. M_{star} relation increases with redshift, which is driven by the rise of SFR/M_{dust} (*i.e.* energy injection rate per unit dust mass). We also notice a slight increase of T_{mw} with M_{star}. This is owing to the decrease of M_{star}/M_{dust} with M_{star} of the MASSIVEFIRE sample. As a result, SFR/M_{dust} slightly increases with M_{star} (*i.e.* SFR/$M_{dust} \propto$ sSFR(M_{star}/M_{dust}) $\propto M_{star}^{0.3}$) at given redshift.

4 (SUB)MILLIMETER BROADBAND FLUXES

A major problem for probing the dust properties in the high-z ($z > 4$) is that most observations of dust emission at such high redshift are limited to a single broadband flux detected by ALMA band 7 or 6. Deriving infrared luminosities and hence SFRs of these $z \gtrsim 4$ objects is very challenging without FIR constraints and depends highly on the assumed *equivalent* dust temperature for the flux-to-luminosity conversion. The same problem also applies to many submm-selected objects at lower redshift ($2 < z < 4$) that do not have *Herschel* FIR coverage. Therefore, an accurate estimate of T_{eqv} of the adopted SED function for different redshifts is critical.

In this section, we will analyse the T_{eqv} distribution of galaxies at $z = 2-6$ with the help of the MASSIVEFIRE sample. Specifically, in Section 4.1, we will examine the redshift evolution of T_{eqv} and its dependence on δ_{dgr}, offering a 'cookbook' for converting between (sub)mm and L_{IR} observations. In Section 4.2, we will compare T_{eqv} with T_{mw} and T_{peak}, and provide a physical interpretation of this dust temperature.

4.1 The flux-to-luminosity conversion

L_{IR} is often extrapolated from a single broadband (sub)mm flux given the lack of additional sub-mm or FIR constraints. A typical approach is to assume that the SED has an OT-MBB (or G-MBB) shape with a chosen value of the dust temperature parameter. However, as we have shown in Figure 3 and discussed in Section 3.1, choosing a dust temperature parameter that is not compatible with the adopted SED fitting function or a fitting function that does not reproduce the shape of the SED can result in significant biases for estimating L_{IR} of a galaxy. By definition, this problem is avoided if the adopted dust temperature is chosen to be T_{eqv}.

With the MASSIVEFIRE sample, we are able to predict the full dust SED for the high-z ($z = 2-6$) objects covering over two orders of magnitude of IR luminosity ($L_{IR} \approx 10^{10} - 10^{12}\ L_\odot$). We predict the observed flux densities at ALMA band 7 ($S_{870\mu m}$) and band 6 ($S_{1.2mm}$) given the SED and redshift as well as L_{IR}. Many of these

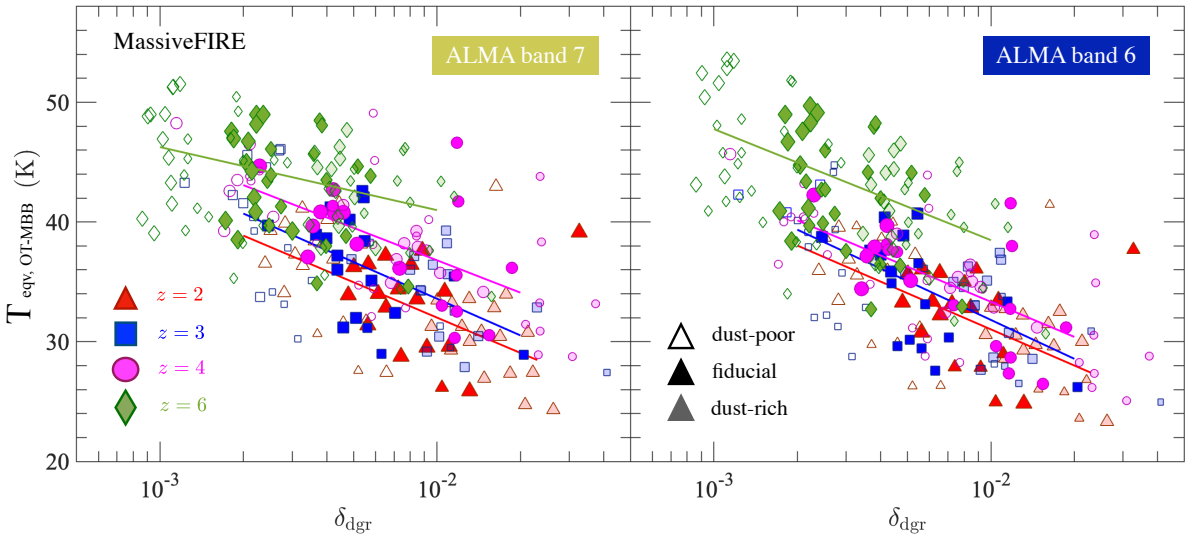

Figure 10. The relation of effective dust temperature ($T_{\rm eqv}$) vs. dust-to-gas ratio ($\delta_{\rm dgr}$) of the $z = 2-6$ MASSIVEFIRE sample. $T_{\rm eqv}$ is the effective dust temperature in the OT-MBB function (Eq. 6, with $\beta = 2.0$) that yields the true $L_{\rm IR}$ of the galaxy from the flux densities at ALMA band 7 at 870 μm (*left panel*) and band 6 at 1.2 mm (*right panel*). The result of $\delta_{\rm dzr} = 0.4$, $\delta_{\rm dzr} = 0.8$, and $\delta_{\rm dzr} = 0.2$ are shown with filled, semi-transparent and unfilled symbols, respectively. $T_{\rm eqv}$ **increases with redshift, and at the same redshift,** $T_{\rm eqv}$ **shows negative correlation with** $\delta_{\rm dgr}$**.**

objects have $S_{870\mu{\rm m}}$ ($S_{1.2{\rm mm}}$) $\gtrsim 0.1$, which are over the 3σ detection limit of ALMA band 6 and 7 using a typical integration time of 1 hour. With the calculated $S_{870\mu{\rm m}}$ (and $S_{1.2{\rm mm}}$) of each galaxy, we find the OT-MBB (with $\beta = 2.0$) and GP-MBB functions (with $\beta = 2.0$, $\lambda_1 = 100$ μm, $\alpha = 2.5$ and the suggested value of $N_{\rm pl}$ by C12), normalised to match their observed flux densities at both ALMA bands, that can predict their true $L_{\rm IR}$. By adjusting the temperature parameter in the fitting function to match both observed sub-mm flux density and true $L_{\rm IR}$, we obtain $T_{\rm eqv}$, *i.e.*, *the value of T necessary for obtaining an accurate estimate of* $L_{\rm IR}$ *from the measured (sub)mm flux densities for each galaxy*.

In Figure 9, we show the relation of $L_{\rm IR}$ against $S_{870\mu{\rm m}}$ (*left panel*) and $S_{1.2{\rm mm}}$ (*right panel*) for the $z = 2-6$ MASSIVEFIRE galaxies. For each redshift, we also show the expected $L_{\rm IR}$ vs. $S_{870\mu{\rm m}}$ (and $S_{1.2{\rm mm}}$) relation using the mean $T_{\rm eqv}$ for galaxies above 0.1 mJy. The latter temperature is provided for the two different ALMA bands and for redshifts $z = 2-6$. We present results for OT-MBB and GP-MBB functional shapes.

There appears to be a clear trend of increasing $T_{\rm eqv}$ with redshift, with either forms of fitting function (GP or OT-MBB) and with either ALMA band 6 or 7. This shows that a higher $T_{\rm eqv}$ is typically needed for deriving $L_{\rm IR}$ of galaxies at higher redshift. Using OT-MBB function, for example, the mean $T_{\rm eqv}$ increases from 34.0 K at $z = 2$ (red triangles) to 44.6 K at $z = 6$ (green diamonds) for ALMA band 7. Applying the typical $T_{\rm eqv}$ for $z = 2$ to a $z = 6$ galaxy will therefore lead to a significant underestimate of $L_{\rm IR}$ by a factor of ~ 4 (Eq 10).

For the same redshift, the normalisation of the $L_{\rm IR}$ vs. $S_{870\,\mu{\rm m}}$ ($S_{1.2{\rm mm}}$) relation depends on dust mass. We explicitly show in Figure 9 the result for dust-rich and dust-poor models. At fixed observed broadband flux density, the $L_{\rm IR}$ of dust-rich galaxies lies systematically below the fiducial model (vice versa for dust-poor galaxies). This result indicates that a galaxy of given observed (sub)mm flux density tends to have lower (higher) $L_{\rm IR}$ if it contains more (less) amount of dust.

This finding can be understood as follows. By increasing the dust mass, both $L_{\rm IR}$ and $S_{870\mu{\rm m}}$ ($S_{1.2{\rm mm}}$) increase but the latter changes by a larger degree. Hence, the normalisation of the relation declines. The increase of $S_{870\mu{\rm m}}$ ($S_{1.2{\rm mm}}$) is mainly driven by dust mass, as $S_{870\mu{\rm m}}$ ($S_{1.2{\rm mm}}$) is linearly scaled to $M_{\rm dust}$ (Eq. 11). On the other hand, the increase of $L_{\rm IR}$ is due to enhanced optical depth — a larger fraction of UV photons gets absorbed by dust and re-emitted in the infrared/submm. A lower $T_{\rm eqv}$ is therefore needed to account for the decrease of the normalisation of the $L_{\rm IR}$ vs. $S_{870\mu{\rm m}}$ ($S_{1.2{\rm mm}}$) relation with increasing dust mass.

We therefore expect a dependence of $T_{\rm eqv}$ on $M_{\rm dust}$, $\delta_{\rm dzr}$, or $\delta_{\rm dgr}$. While it is difficult to constrain $M_{\rm dust}$ and $\delta_{\rm dzr}$ observationally, the dust-to-gas ratio, $\delta_{\rm dgr} = M_{\rm dust}/M_{\rm mol}$ can be inferred using the empirical $\delta_{\rm dgr} - Z_{\rm gas}$ scaling relation (Leroy et al. 2011; Magdis et al. 2012). In principle, $Z_{\rm gas}$ (the galaxy gas-phase metallicity) can be measured with optical and/or FIR emission lines, or crudely estimated given the galaxy stellar mass via the mass–metallicity relation. Possible methods for constraining $Z_{\rm gas}$ of high-z galaxies are discussed in more depth in Section 5.

Figure 10 shows the relation between $T_{\rm eqv}$ and $\delta_{\rm dgr}$ of the $z = 2-6$ MASSIVEFIRE sample. At fixed redshift, there is a clear negative correlation between the derived $T_{\rm eqv}$ and $\delta_{\rm dgr}$. Using all the $z = 2-6$ objects with $S_{870\mu{\rm m}}$ ($S_{1.2{\rm mm}}$) > 0.1 mJy, including the data for $\delta_{\rm dzr} = 0.2-0.8$, we perform a multiple linear regression analysis

$$\log\left(T_{\rm eqv}/25\,{\rm K}\right) = a + b\log\left(\delta_{\rm dgr}/0.01\right) + c\log\left(1+z\right). \quad (15)$$

We present the best-fit regression parameters a, b and c for ALMA band 6 and 7, and for OT-MBB and GP-MBB functions in Table 1. These derived scaling relations are useful for converting a measured (sub)mm flux density into $L_{\rm IR}$, provided redshift and dust-to-gas ratio are known or can be estimated. Adding $M_{\rm star}$ as a predictor variable results in a regression coefficient for the $M_{\rm star}$ term being consistent with zero. Replacing the redshift dependence with a dependence on $M_{\rm star}$ leads to a decreased goodness-of-fit for $T_{\rm eqv}$.

4.2 The equivalent dust temperature

$T_{\rm eqv}$ depends on redshift and $\delta_{\rm dgr}$ in a clear and systematic manner, see Table 1. For the OT-MBB functional shape, for example, $T_{\rm eqv}$

Table 1. Scaling relations between $T_{\rm eqv}$, $\delta_{\rm dgr}$ and redshift. $z = a + b \times x + c \times y$, where $z = \log(T_{\rm eqv}/25\,{\rm K})$, $x = \log(\delta_{\rm dgr}/0.01)$ and $y = \log(1+z)$.

	OT$^{i)}$ (band 7)	OT$^{i)}$ (band 6)	GP$^{ii)}$ (band 7)	GP$^{ii)}$ (band 6)
a	0.04 ± 0.03	0.01 ± 0.02	0.06 ± 0.05	0.02 ± 0.05
b	−0.10 ± 0.02	−0.12 ± 0.01	−0.14 ± 0.02	−0.17 ± 0.04
c	0.18 ± 0.06	0.19 ± 0.04	0.25 ± 0.03	0.28 ± 0.09

$^{i)}$ With fixed $\beta = 2.0$.
$^{ii)}$ With $\lambda_1 = 100\,\mu$m, $\beta = 2.0$, $\alpha = 2.5$ and the fiducial $N_{\rm pl}$ by Casey (2012).

scales as $\propto (1+z)^{0.2}\delta_{\rm dgr}^{-0.12}$. This means that by applying a typical $T_{\rm eqv}$ for $z = 2$ to a $z = 6$ galaxy would lead to an underestimate of $L_{\rm IR}$ by about a factor of ~ 3 (Eq. 10). Also, at a given redshift, an order-of-magnitude increase of $\delta_{\rm dgr}$ corresponds to a ~ 0.12 dex decrease of the best-fitting $T_{\rm eqv}$. This corresponds to a decrease of $L_{\rm IR}$ by a factor of ~ 4 (Eq. 10). Therefore, not taking the correlation of $T_{\rm eqv}$ with redshift and $\delta_{\rm dgr}$ into account can potentially lead to significant biases in the $L_{\rm IR}$ (and hence SFR) estimates.

The scaling $T_{\rm eqv} \propto (1+z)^{0.2}$ is quantitatively similar to the one for $T_{\rm peak}$ (Eq. 12), meaning that $T_{\rm eqv}$ also evolves more quickly with redshift compared to $T_{\rm mw}$ (see *left panels* of Figure 7). A natural question arises — what drives the evolution of $T_{\rm eqv}$ with redshift and $\delta_{\rm dgr}$?

To answer this question, we show in Figure 11 the $T_{\rm eqv}$ vs. $T_{\rm mw}$ (*upper panel*) and $T_{\rm eqv}$ vs. $T_{\rm peak}$ (*lower panel*) relations of the MASSIVEFIRE sample at $z = 2-6$. In this figure, $T_{\rm eqv}$ is calculated using an OT-MBB functional form (with fixed $\beta = 2.0$) given a flux density at ALMA band 6. Using ALMA band 7 or a different form of MBB function results in qualitatively similar results and thus does not effect our conclusions.

It is clear from Figure 11 that $T_{\rm eqv}$ is more strongly correlated with $T_{\rm peak}$ than $T_{\rm mw}$, either by looking at the $z = 2-6$ sample as a whole, or each individual redshift. For each redshift, $T_{\rm peak}$ scales approximately linearly with $T_{\rm eqv}$, with a high Pearson correlation coefficient $r \sim 0.95$. In contrast, the relation between $T_{\rm mw}$ and $T_{\rm eqv}$ is sub-linear and shows large scatter. As shown in the *upper panel*, galaxies with similar $T_{\rm mw}$ can have very different $T_{\rm eqv}$ ($\Delta T_{\rm eqv} > 10$ K) and thus a large range of $L_{\rm IR}/S$ ratios (Eq. 10).

To understand the origin of the scatter in $T_{\rm eqv}$ and fixed $T_{\rm mw}$, we selected two galaxies from the MASSIVEFIRE sample with similar $T_{\rm mw}(\approx 30\,{\rm K})$, one from $z = 2$ and the other from $z = 6$, and study their SEDs and their $T_{\rm eqv}$ in more detail. The two galaxies are marked in both panels of Figure 11 by yellow asterisks, and their SEDs are presented in Figure 3. The $z = 6$ galaxy has $T_{\rm eqv,\,OT-MBB} = 49.1$ K which is about 14 K higher than the $z = 2$ galaxy.

Figure 3 showed that the two galaxies have different SED shapes at short wavelengths. The $z = 6$ galaxy shows more prominent MIR emission due to its more active recent star formation. Its sSFR ($= 4.3 \times 10^{-9}\,M_\odot\,{\rm yr}^{-1}$) is about 7 times higher than that of the $z = 2$ galaxy. Young star clusters in this high-redshift galaxy efficiently heat the dense, surrounding dust, which boosts the MIR emission and thus leads to a relatively high $T_{\rm peak}(= 44.6$ K) to account for the more prominent MIR emission of this galaxy. Furthermore, the $z = 6$ galaxy is less dust-enriched than the $z = 2$ galaxy (having only 1/7 of dust mass), and its SFR/$M_{\rm dust}$ ratio is roughly 3.5 times higher.

The increased SFR/$M_{\rm dust}$ ratio would leave an imprint on the

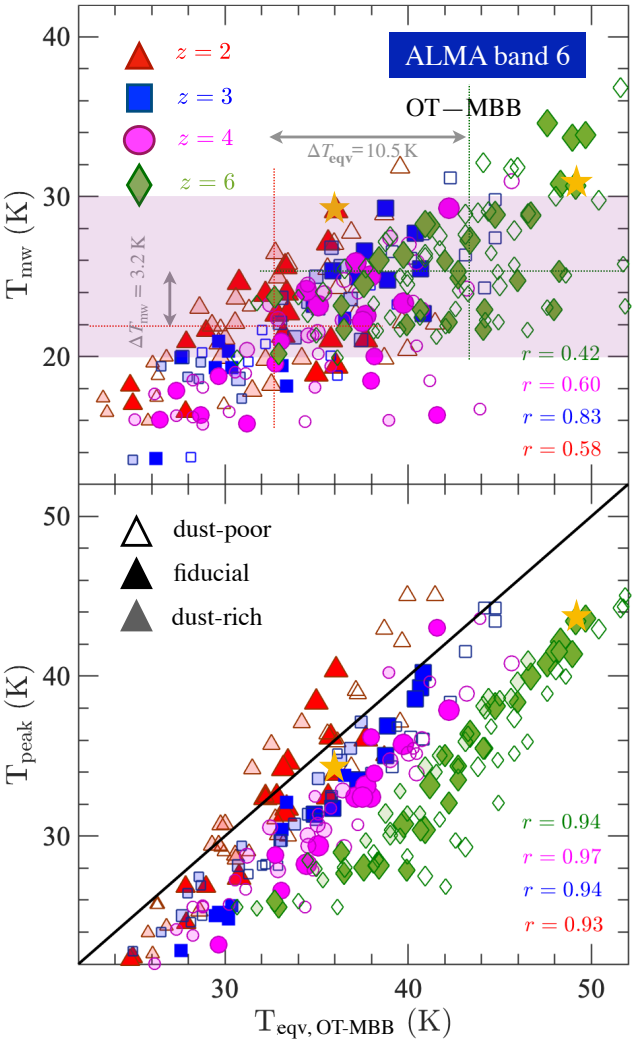

Figure 11. The relation between $T_{\rm mw}$ (upper panel) vs. $T_{\rm eqv,\,OT-MBB}$ and $T_{\rm peak}$ (lower panel) vs. $T_{\rm eqv,\,OT-MBB}$ of the $z = 2-6$ MASSIVEFIRE galaxies, where $T_{\rm eqv,\,OT-MBB}$ is the equivalent dust temperature for the adopted OT-MBB function (Eq. 6, with fixed $\beta = 2.0$) that yields the right $L_{\rm IR}$ from $S_{1.2{\rm mm}}$. In the *upper panel*, the two horizontal dotted lines mark the mean $T_{\rm mw}$ of the $z = 2$ (red) and $z = 6$ (green) samples, while the two vertical dotted lines mark their mean $T_{\rm eqv,\,OT-MBB}$. The violet shaded box shows $T_{\rm mw} = 25 \pm 5$ K, where $T_{\rm mw} = 25$ K is the suggested dust temperature for estimating dust/gas mass using the RJ approach by Scoville et al. (2016) (Section 3.4.1). The two yellow asterisks in each panel mark the selected $z = 2$ (left) and $z = 6$ (right) galaxies. Their SEDs are shown in Figure 3. The two galaxies have similar $T_{\rm mw}$, but very different $T_{\rm peak}$ and $T_{\rm eqv}$. $T_{\rm eqv,\,1.2mm}$ exhibits stronger correlation with $T_{\rm peak}$ than $T_{\rm mw}$.

temperature of the diffuse dust if the heat budget of the young stars were evenly distributed in the ISM dust. However, the bulk of the diffuse cold dust is clearly not heated efficiently as the two galaxies have almost the same $T_{\rm mw}$ (29.1 K vs. 30.7 K). A number of factors can influence how efficiently the bulk of the dust is heated, such as the spatial distribution of dust in galaxy and the optical depth in vicinity of the star-forming cores. These conditions can be significantly different among galaxies and therefore $T_{\rm mw}$ is not expected to be well correlated with $T_{\rm peak}$ (see the *upper right panel* of Figure 7). This example strongly indicates that a 'two-phase' picture

of ISM dust is needed to account for the discrepancy between $T_{\rm mw}$ and $T_{\rm peak}$, see Figure 12.

Clearly, $T_{\rm eqv}$ depends on the observed frequency band and the exact form of the MBB function. As is shown in Table 1 (and Figure 9), $T_{\rm eqv}$ is slightly higher if the SED shape is assumed to be well described by a GP-MBB function vs an OT-MBB. Furthermore, with ALMA band 7, $T_{\rm eqv}$ is slightly higher, indicating that a steeper MBB function is needed to recover the true $L_{\rm IR}$ when flux density is measured at shorter wavelength. This also explains why the normalisation of the $T_{\rm peak}$ vs. $T_{\rm eqv}$ relation declines with redshift (*lower panel* of Figure 11). As $T_{\rm eqv}$ depends both on the specific form of MBB function and the observed wavelength, $T_{\rm eqv}$ should *not* be interpreted as a physical temperature but rather understood as a parametrisation of SED shape.

Finally, it may appear reasonable to use sSFR as a predictor variable instead of $(1+z)$, given that the former depends strongly on redshift (Figure 8) and is physically linked to the amount of hot dust in galaxies. However, the mapping between observed (sub)mm flux and rest-frame SED introduces an explicit redshift dependence on $T_{\rm eqv}$. Therefore, the $(1+z)$ term in Eq. 15 accounts both (indirectly) for the cosmic time dependence of the sSFR and (directly) for the redshift of electromagnetic radiation.

5 DISCUSSION

5.1 Deriving $M_{\rm dust}$

Many dust-enshrouded galaxies at high redshift ($z > 2$) have been detected at (sub)mm wavelengths in the past years, thanks to the unprecedented sensitivity of ALMA. These (sub)mm-detected objects often lack a reliable measure of FIR photometry and many are extremely faint at UV/optical wavelengths (*e.g.* Daddi et al. 2009; Walter et al. 2012; Riguccini et al. 2015; Franco et al. 2018b). A reliable estimate of their dust mass from full SED fitting is often not possible.

In the optically-thin regime, the flux density in the RJ tail has a simple analytic form (Eq. 11), and $M_{\rm dust}$ can be derived from the flux density given $T_{\rm mw}$ (Section 3.4.1). However, it is difficult to constrain $T_{\rm mw}$ of high-redshift galaxies when individual star-forming regions are not resolved.

Fortunately, we find that $T_{\rm mw}$ does not strongly vary from galaxy to galaxy. This is noteworthy, given that our sample spans a wide range of cosmic time ($z = 2-6$), stellar mass ($M_{\rm star} = 10^9 - 10^{12}\,M_\odot$), sSFR ($10^{-10} - 10^{-8}\,{\rm yr}^{-1}$), and IR luminosities ($L_{\rm IR} = 10^9 - 3\times10^{12}\,L_\odot$). In particular, 68% (*i.e.* 1σ) of the galaxies in our sample have mass-weighted dust temperatures $T_{\rm mw} = 25\pm5$ K, corresponding to a 20% uncertainty of estimating the dust mass as the mass estimates scale linearly with $T_{\rm mw}$, while 90% of our sample lies within $T_{\rm mw} = 25\pm8$ K (32% uncertainty of $M_{\rm dust}$). Our findings support the empirical approach of adopting a constant $T_{\rm mw} = 25$ K to estimate the ISM mass of high redshift galaxies via Eq. 11 and $\delta_{\rm dgr}$ (Scoville et al. 2016).

While adopting a constant $T_{\rm mw}$ is a good assumption to first order, and the only option if the (sub)mm flux density is measured at only a single wavelength, additional constraints on the SED may help to determine $T_{\rm mw}$ and improve the accuracy of measuring ISM masses. Specifically, in Section 3.4.3, we show that $T_{\rm mw}$ is well correlated with $L_{\rm IR}$ and that the redshift evolution of the $L_{\rm IR}$ vs. $T_{\rm mw}$ relation is driven by the evolving dust mass. In fact, $L_{\rm IR}$, $M_{\rm dust}$ and $T_{\rm mw}$ follow a tight scaling relation (Eq. 13) for $T_{\rm mw} \gg T_{\rm CMB}$. Hence, given $S \propto M_{\rm dust} T_{\rm mw}$, it should be possible to simultaneously infer $M_{\rm dust}$ and $T_{\rm mw}$ from a combined measurement of S and $L_{\rm IR}$.

Recent studies have shown that the broadband rest-frame 8 μm luminosity, L_8, is linearly correlated with $L_{\rm IR}$ over a wide range of $L_{\rm IR}$ (Elbaz et al. 2011; Magdis et al. 2013). Current observational constraints on IR8 are currently limited to $z \lesssim 2$. The unprecedented sensitivity of the Mid-Infrared Instrument (MIRI) on board the upcoming James Webb Space Telescope (JWST), covering the wavelength range of 5 to 28 μm, will significantly enlarge the sample size of distant galaxies with measured MIR broadband spectroscopy. Together with the MIR and FIR instruments on board SPICA, JWST could potentially improve the measurement of the mid-to-total infrared colour, $L_{\rm IR}/L_{\rm MIR}$, where $L_{\rm MIR}$ is rest-frame MIR broadband luminosity, to higher redshift and to fainter luminosities. We thus propose to use $L_{\rm MIR}$ to infer $L_{\rm IR}$ for many (sub)mm-detected galaxies at $z\lesssim4$ that currently have no constraint on SED shape near the emission peak.

Hence, we propose to derive $M_{\rm dust}$ (as well as $T_{\rm mw}$) of high-redshift galaxies by combining mid-infrared (e.g., from JWST) and far-infrared/submm (e.g., ALMA) data sets. Specifically, by combining Eq. 11 and 13, we obtain

$$\log\left(\frac{M_{\rm dust}}{M_\odot}\right) = 1.23\log\left(\frac{S}{\rm mJy}\right) - 0.23\log\left(\frac{L_{\rm IR}}{L_\odot}\right) + \mathcal{F}(z)$$
$$\text{or}\quad M_{\rm dust} \propto \left(\frac{S}{L_{\rm IR}}\right)^{0.23} S, \tag{16}$$

where $\mathcal{F}(z) = -0.85 + 1.23\log(\psi(z)\Gamma_{\rm RJ})$ and $\psi(z)$ has the unit of mJy $M_\odot^{-1}$ K^{-1}. Assuming that $L_{\rm IR} = \alpha\, L_{\rm MIR}$ (Magdis et al. 2013), we can rewrite the above equation as

$$\log\left(\frac{M_{\rm dust}}{M_\odot}\right) = 1.23\log\left(\frac{S}{\rm mJy}\right) - 0.23\log\left(\frac{L_{\rm MIR}}{L_\odot}\right) + \mathcal{G}(z) \tag{17}$$

where $\mathcal{G}(z) = -0.23\log\alpha + \mathcal{F}(z)$. In general, $\Gamma_{\rm RJ}$ is a function of T and Eqs. 11 & 17 need to be solved numerically.

It may be possible to improve on this simple approach further, e.g., to account for dependencies of α on sSFR and metallicity (*e.g.* Nordon et al. 2012; Schreiber et al. 2018), with the help of empirical scaling relationships. In particular, Schreiber et al. (2018) found a non-linear scaling of α with sSFR. By combining this empirical relation with sSFR $\propto (L_{\rm MIR}/M_{\rm star})\times\alpha$, one can constrain $L_{\rm IR}$ directly from measurements of $M_{\rm star}$ and $L_{\rm MIR}$.

According to Eq. 16, a factor of 2 uncertainty in $L_{\rm IR}$ translates into $\sim$ 20% uncertainty in the derived dust mass, i.e., matches the intrinsic level of error of the constant $T_{\rm mw} = 25$ K method (Scoville et al. 2016). Hence, increasing complexity by deriving $T_{\rm mw}$ and $M_{\rm dust}$ from $L_{\rm IR}$ and S will only be beneficial if $L_{\rm IR}$ can be constrained to within a factor of 2 or better.

5.2 Calibrating $T_{\rm eqv}$ with dust-to-gas ratio $\delta_{\rm dgr}$

Adopting $T_{\rm eqv}$ and an SED shape is another way to estimate the IR luminosity from submm fluxes, see Section 4.2. Hence, if $T_{\rm eqv}$ is known, it is possible to use the approach described in the previous section to infer dust masses and mass-weighted temperatures. This could be a particularly useful approach at $z > 4$, where the potential MIR diagnostics redshift out of the wavelengths accessible by JWST.

Fig. 10 showed that $T_{\rm eqv}$ is anti-correlated with $\delta_{\rm dgr}$ at fixed redshift. Specifically, an order-of-magnitude decrease of $\delta_{\rm dgr}$ translates to $\sim$ 0.12 dex increase of required $T_{\rm eqv}$, and hence a factor of

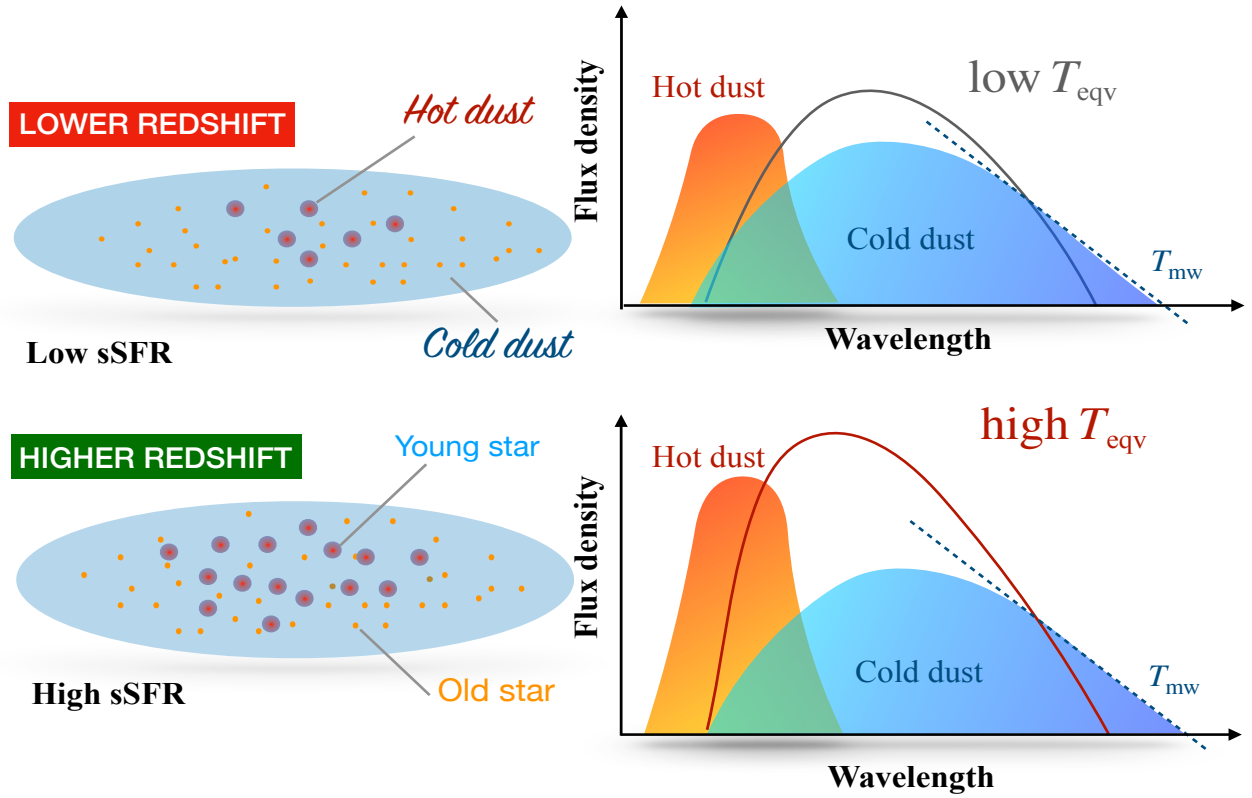

Figure 12. Schematic figure for the 'two-phase' model of ISM dust and the implication on the dust SED. Higher-redshift galaxies have higher sSFR and more young ($t_{age} \lesssim 10$ Myrs) star clusters efficiently heat the dense dust in vicinity of the star-forming regions to high temperature. This hot dust component boosts the overall SED of galaxy at MIR. A higher equivalent temperature (T_{eqv}) is thus needed to account for the more prominent MIR emission of galaxies at higher redshift. T_{eqv} is not well correlated with the mass weighted temperature (T_{mw}) of galaxy. T_{mw} is determined by the cold dust component and it sets the slope of the RJ tail.

~ 4 increase of L_{IR} (Eq. 10). Therefore, having an estimate of δ_{dgr} of high-redshift galaxies can largely improve the accuracy of estimated L_{IR}.

Observationally, δ_{dgr} can be estimated through the $\delta_{dgr} - Z$ scaling relations (Leroy et al. 2011; Magdis et al. 2012), and traditionally, the observed gas-phase oxygen abundance is used as a proxy for gas metallicity. It is derived using the ratios between strong (rest-frame) optical nebular emission lines and with calibration on theoretical models (*e.g.* Kewley & Dopita 2002; Kewley & Ellison 2008; Zahid et al. 2011; Steidel et al. 2014). However, this method can only be used for galaxies up to $z \sim 3$, above which the emission lines redshift out of the wavelengths of the current ground-based near-IR spectrographs. To overcome this difficulty, Rigopoulou et al. (2017) have recently proposed a new method of using the (rest-frame) FIR [OIII] 88 μm/[NII] 122 μm line ratio for probing the gas-phase metallicities of galaxies at earlier epochs, where both characteristic lines shift to the submm range that is accessible with ALMA. Using the previously reported FIR line measurements of a sample of local normal and star-forming galaxies by the *Infrared Space Observatory* (ISO, Kessler et al. 1996), Rigopoulou et al. (2017) find that the derived galaxy mass-metallicity relation is consistent with the result derived using optical emission lines (Tremonti et al. 2004). The gas metallicities of a number of $z = 2 \sim 3$ submm-luminous galaxies derived using *Herschel* measurements are also in good agreement with the high-z relationships previously derived by Maiolino et al. (2008) and Mannucci et al. (2010). These results suggest that FIR emission lines could be powerful tool for estimating gas metallicity, and hence δ_{dgr} of galaxies at $z > 4$.

5.3 The sub-resolution structure of the birth-clouds

Observational evidence has indicated that young star clusters reside in dense dusty birth-clouds (*e.g.* Calzetti et al. 1997; Tuffs et al. 2004; Wild et al. 2011; Price et al. 2014; Koyama et al. 2015). To check the uncertainty arising from potentially unresolved small-scale ISM structure, we have repeated the analysis presented in this paper with additional RT analysis by SKIRT as Liang et al. (2018), where we include a sub-grid model for birth-clouds embedding the young stars (our 'alternative' RT model). We summarise the detail of this sub-grid model and the main results from this model in this subsection.

In brief, all the young star particle of a galaxy that has formed less than 10 Myrs ago is assigned a MAPPINGSIII source SED (Groves et al. 2008). MAPPINGSIII SED templates are parameterised by the SFR and the metallicity of the star-forming regions, the pressure of the ambient ISM, the HII region compactness (log C), and the covering fraction of the associated PDR (f_{pdr}).

To explore how our results depend on this choice, the *upper* and *lower* panels in Figure 13 show the overall SED of one of our galaxies for different values of log C and f_{pdr}, respectively. As log C increases, the birth-clouds become more compact and the dust associated with the clouds attain higher mean temperature because of the stronger incident radiation onto dust grains. The source SED of this dust component (shown with dashed lines) shifts to

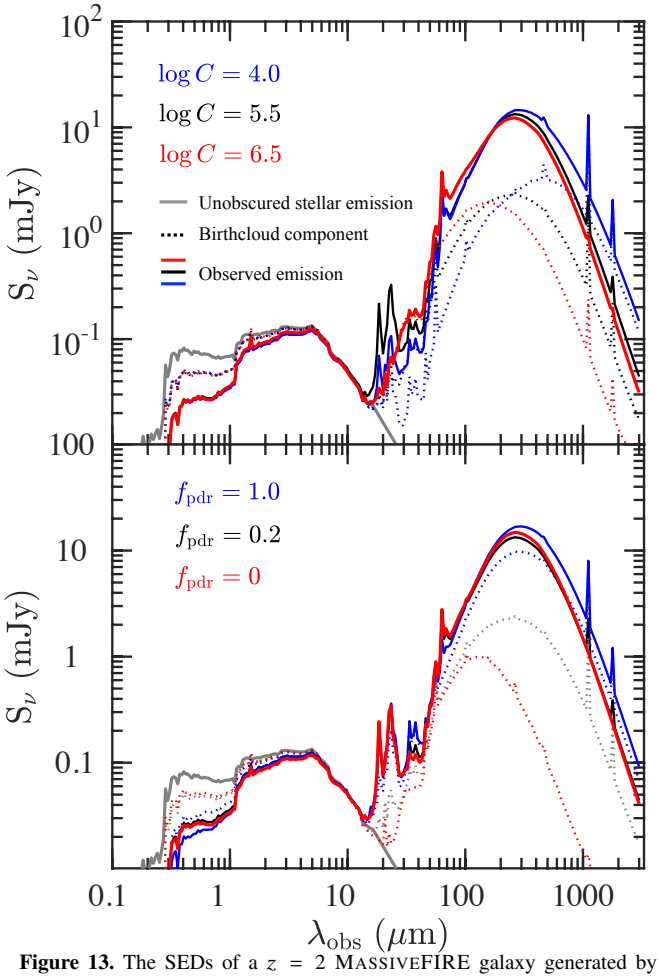

Figure 13. The SEDs of a $z = 2$ MASSIVEFIRE galaxy generated by different dust models. In the left panel, we show the observed SEDs for $\log C = 6.5$ (red), 5.5 (black) and 4.0 (blue) with fixed $f_{\rm pdr}$ (= 0.2). In the right panel, we show the result for $f_{\rm pdr} = 0$ (red), $f_{\rm pdr} = 0.2$ (black) and $f_{\rm pdr} = 1.0$ (blue) with fixed $\log C$ (= 5.5). In each panel, the grey curve shows the intrinsic stellar emission, while the solid red, black and blue curves show the observed SEDs, each corresponding to a different dust model. Source SEDs from birth-clouds associated with the star forming regions are shown with dotted lines with the corresponding colour for each model.

shorter wavelength, and so does the overall SED of the galaxy. $f_{\rm pdr}$ is a measure of the survival timescale of birth-clouds (Jonsson et al. 2010). Increasing $f_{\rm pdr}$ results in a larger fraction of the stellar emission being absorbed by dust in the birth-clouds, which results in more energy being re-emitted as IR light. The mean dust temperature, however, decreases. Hence, a higher $f_{\rm pdr}$ leads to higher $L_{\rm IR}$ and an emission peak shifted to longer wavelengths.

The sub-grid model has minor impact on $T_{\rm mw}$ of galaxies. $T_{\rm mw}$ increases with $\log C$ at fixed $f_{\rm pdr}$, and decreases with $f_{\rm pdr}$ at fixed $\log C$. The reason is that the photons emitted from the birth-clouds are more energetic if the birth-clouds are more compact (higher $\log C$) and less dust-obscured (low $f_{\rm pdr}$). But the resulting difference of $T_{\rm mw}$ is typically no more than ±1 K (±5%) by exploring the parameter space of the MappingsIII model.

$T_{\rm peak}$, however, is more sensitive to the uncertainty of the small-scale ISM structure. $T_{\rm peak}$ is typically higher with increasing $\log C$ (decreasing $f_{\rm pdr}$). In some cases, especially for strongly star-forming galaxies, $T_{\rm peak}$ can differ by much as 10 K when the MappingsIII parameters are varied. For the $z = 2$ MassiveFIRE sample, $\log C = 6.5$ (max) leads to a median $T_{\rm peak}$ higher than $\log C = 4.0$ (min) by about 3 K, and $f_{\rm pdr} = 1.0$ (max) yields a median $T_{\rm peak}$ lower than $f_{\rm pdr} = 0$ (min) by about 2.5 K. Uncertainty of the small-scale ISM conditions could introduce scatter in the observed $T_{\rm peak}$ vs. $L_{\rm IR}$ relation in addition to galaxy-by-galaxy variations of $\delta_{\rm dzr}$.

Including the sub-grid birth-cloud model strengthens the correlation between $T_{\rm peak}$ (and $T_{\rm eqv}$) and sSFRs of galaxies. By pre-processing starlight in birth-clouds, the range of the physical conditions surrounding star-forming regions is reduced. We note, however, that none of the trends reported in this paper change on a qualitative level by including or excluding the MappingsIII birth-cloud model.

6 SUMMARY AND CONCLUSION

In this paper, we study dust temperatures of high-redshift galaxies and their scaling relationships with the help of cosmological zoom-in simulations and dust RT modelling. Our sample consists of massive ($M_{\rm star} > 10^{10}\ M_\odot$) $z = 2-6$ galaxies extracted from the MASSIVEFIRE suite (Feldmann et al. 2016; Feldmann et al. 2017), a set of cosmological hydrodynamic zoom-in simulations from the FIRE project (Hopkins et al. 2014). The sample encompasses 18 central galaxies at $z = 2$ and their most massive progenitors up to $z = 6$, together with a disjoint set of 11 central galaxies at $z = 6$. We generate FIR-to-mm broadband fluxes and spectra for our galaxy sample with SKIRT.

We explicitly define and discuss four different dust temperatures that are commonly used in the literature, $T_{\rm mw}$, $T_{\rm peak}$, $T_{\rm eff}$ and $T_{\rm eqv}$. $T_{\rm mw}$ is the physical, mass-weighted temperature that can be extracted from RT analysis, but is often not easily accessible to observations. $T_{\rm eff}$ and $T_{\rm peak}$ are derived from SED fitting: $T_{\rm eff}$ is the T parameter in the best-fit modified blackbody function and $T_{\rm peak}$ is the inverse of emission peak wavelength. These two are the temperatures that are often adopted for analysing large statistical sample of galaxies by observational studies. And finally, $T_{\rm eqv}$ is the temperature one needs to convert single (sub)mm data to total IR luminosity based on an assumed SED shape.

The main findings of this paper are:

- FIRE simulations together with RT processing successfully reproduce $T_{\rm peak}$ of $z = 2$, $L_{\rm IR} \gtrsim 10^{11}\ L_\odot$ galaxies, in good agreement with recent observations (Figure 4). The observational data shows large scatter, which may be driven by galaxy-to-galaxy variations of $\delta_{\rm dzr}$ as well as local variations in the physical conditions of unresolved birth-clouds embedding young star clusters (Section 3.3).
- $T_{\rm mw}$ is only weakly correlated with $T_{\rm peak}$ over $z = 2-6$ (Figure 7). The former sets the slope of the RJ tail (Figure 3), and is the temperature needed for estimating dust and gas mass of distant galaxies (Figure 5). Using $T_{\rm peak}$, or $T_{\rm eff}$ (*e.g.* derived from full SED fitting), which is strongly correlated with $T_{\rm peak}$, can lead to a systematic bias/error of the derived dust/gas mass, and may lead to an inaccurate interpretation of the star-forming conditions in high-redshift galaxies (Section 3.4.1).
- $T_{\rm peak}$ is well correlated with sSFR ($r \sim 0.7$) (Figure 7). Recently formed stars efficiently heat the dense, warm dust in the close vicinity of star-forming regions. The emission from this warm dust component boosts the overall dust SED at MIR, and helps to shift the emission peak to shorter wavelength (Figure 12). $T_{\rm mw}$ is less well correlated with sSFR ($r \sim 0.5$) and the scaling relation shows a flatter slope ($\Delta T_{\rm mw} \propto {\rm SB}^{4.2}$ vs.

$\Delta T_{\rm peak} \propto {\rm SB}^{10.9}$). The bulk of the cold diffuse dust is not as effectively heated as the warm dust component (Section 3.4.4).

- $T_{\rm peak}$ scales as $(1+z)^{0.22}$ at fixed $L_{\rm IR}$ between $z = 2-6$ driven by the increasing sSFR at higher redshift, which is consistent with recent observations (Section 3.4.3). $T_{\rm mw}$ evolves only weakly with redshift at fixed $L_{\rm IR}$ at $z = 2-6$ (Figure 7).
- Of the galaxies in our sample, 68% have mass-weighted dust temperatures $T_{\rm mw} = 25 \pm 5$ K (Figure 11). This temperature range corresponds to an uncertainty of 20% in estimating $M_{\rm dust}$ from a single submm band. Furthermore, 90% of our sample lies within $T_{\rm mw} = 25 \pm 8$ K. Our findings support the empirical approach of adopting a constant $T_{\rm mw} = 25$ K to estimate the ISM mass of high redshift galaxies (Scoville et al. 2016).
- $T_{\rm mw}$ is well correlated with $L_{\rm IR}$ at $T_{\rm mw} \gg T_{\rm CMB}$ at a given redshift (Figure 7). The normalisation of this relation evolves weakly with redshift but the slope does not change. At higher redshift, galaxies of the same $L_{\rm IR}$ have higher $T_{\rm mw}$ but lower $M_{\rm dust}$. Using the $z = 2-6$ sample, we derive the scaling relation $L_{\rm IR} \propto M_{\rm dust}^{1.0} T_{\rm mw}^{5.4}$, which appears to be shallower than the classical $L_{\rm IR} \propto M_{\rm dust} T^{4+\beta}$ relation expected from the optically-thin assumption (Section 3.4.3).
- We propose to use this scaling relation to derive $M_{\rm dust}$ (and $T_{\rm mw}$) of high-redshift (sub)mm-detected galaxies, assuming that their $L_{\rm IR}$ can be constrained, for example, via the mid-IR luminosity probed by the *Spitzer* telescope and the upcoming JWST. We showed that this method improves over the $T_{\rm mw} = 25$ K approach if $L_{\rm IR}$ can be constrained to within a factor of 2 or better (Section 5.1).
- $T_{\rm eqv}$ increases with redshift, meaning that a higher temperature is needed to convert observed (sub)mm broadband fluxes to $L_{\rm IR}$ (and hence SFRs) of galaxies at higher redshift. $T_{\rm eqv}$ is tightly correlated ($r \sim 0.95$) with $T_{\rm peak}$, a much stronger correlation than with $T_{\rm mw}$ (Figure 11). In particular, two galaxies at different redshifts can have very different $T_{\rm eqv}$ ($\Delta T_{\rm eqv} > 10$ K) but similar $T_{\rm mw}$ (Section 4).
- We find an anti-correlation between $T_{\rm eqv}$ and the dust-to-gas ratio, $\delta_{\rm dgr}$. Hence, at a given redshift, dust-poorer galaxies need, on the average, a higher $T_{\rm eqv}$ for the (sub)mm-flux-to-IR-luminosity conversion. We express $T_{\rm eqv}$ as a power-law function of $\delta_{\rm dgr}$ and $(1+z)$, and perform linear regression analysis using the MASSIVEFIRE sample at $z = 2-6$. The best-fit parameters of the scaling relation are provided in Table 1. We present the result for both ALMA band 6 and 7. We propose to apply the scaling relation of $T_{\rm eqv}$ to more accurately convert between (sub)mm flux and IR luminosity (and SFR) of high-redshift galaxies (Section 4).

To summarize our results, we find that the observationally-derived temperatures, in particular, $T_{\rm peak}$, generally differ from $T_{\rm mw}$. $T_{\rm peak}$ shows a steeper slope and a stronger correlation with sSFR, and evolves more quickly with redshift compared with $T_{\rm mw}$. We also find that $T_{\rm eqv}$ is more strongly correlated with $T_{\rm peak}$ than with $T_{\rm mw}$.

The difference between $T_{\rm peak}$ and $T_{\rm mw}$ may be understood by a 'two-phase' picture of ISM dust. $T_{\rm mw}$ is set by the diffuse, cold dust component which dominates the total dust mass, while $T_{\rm peak}$ is also influenced by the dense, warm dust component in the close vicinity of young star clusters. The former component is typically heated less effectively by young stars than the latter component so that $T_{\rm peak}$ and $T_{\rm mw}$ are not well correlated with each other.

The increase of $T_{\rm eqv}$ with redshift is consistent with recent observational evidence, including low number counts of (sub)mm sources in ALMA blind surveys (Casey et al. 2018b, and references therein) and the unusual IRX-β relation of high-redshift galaxies (Capak et al. 2015; Bouwens et al. 2016, *cf.* Ma et al. 2019). However, as we argue in this paper, the rise of $T_{\rm eqv}$ with redshift is not simply a sign of dust being hotter at higher redshift, but it reflects the change in SED shape. In particular, higher $T_{\rm eqv}$ is often a consequence of a more prominent MIR emission of galaxies at higher redshift, resulting from more active star formation. However, as $T_{\rm mw}$ evolves only weakly between $z = 2$ and $z = 6$, the temperature of the majority of the dust component ($\sim T_{\rm mw}$) does not significantly change despite the change in $T_{\rm eqv}$. In this sense, dust in galaxies with higher $T_{\rm eqv}$ is not necessarily *physically* hotter.

In conclusion, dust temperature is important for estimating and probing key physical properties (*e.g.* dust/gas mass, IR luminosity) and ISM conditions of high-redshift galaxies. A proper interpretation of dust temperatures and their scaling relationships requires taking into account the differences between temperatures derived from the SED shape and the physical, mass-weighted dust temperature. Upcoming facilities, such as JWST and SPICA, will significantly improve our capability of constraining key dust properties of galaxies in the distant Universe.

ACKNOWLEDGEMENTS

LL would like to acknowledge the stimulating atmosphere during the Munich Institute for Astro- and Particle Physics (MIAPP) 2018 programme *the Interstellar Medium of High Redshift Galaxies* that helped to improve the quality of this manuscript. The visit was supported by the MIAPP of the DFG cluster of excellence "Origin and Structure of the Universe". RF acknowledges financial support from the Swiss National Science Foundation (grant no 157591). Simulations were run with resources provided by the NASA High-End Computing (HEC) Program through the NASA Advanced Supercomputing (NAS) Division at Ames Research centre, proposal SMD-14-5492. Additional computing support was provided by HEC allocations SMD-14-5189, SMD-15-5950, by NSF XSEDE allocations AST120025, AST150045, by allocations s697, s698 at the Swiss National Supercomputing Centre (CSCS), and by S3IT resources at the University of Zurich. DK acknowledges support from the NSF grant AST-1715101 and the Cottrell Scholar Award from the Research Corporation for Science Advancement. CAFG was supported by NSF through grants AST-1517491, AST-1715216, and CAREER award AST-1652522; by NASA through grant 17-ATP17-0067; by STScI through grant HST-AR-14562.001; and by a Cottrell Scholar Award from the Research Corporation for Science Advancement. PFH was supported by an Alfred P. Sloan Research Fellowship, NASA ATP Grant NNX14AH35G, and NSF Collaborative Research Grant #1411920 and CAREER grant #1455342. EQ was supported in part by a Simons Investigator Award from the Simons Foundation and by NSF grant AST-1715070. The Flatiron Institute is supported by the Simons Foundation.

REFERENCES

Aravena M., et al., 2016, ApJ, 833, 68
Armus L., et al., 2009, PASP, 121, 559
Baes M., Camps P., 2015, Astronomy and Computing, 12, 33
Baes M., Verstappen J., De Looze I., Fritz J., Saftly W., Vidal Pérez E., Stalevski M., Valcke S., 2011, ApJ Supplement Series, 196, 22

Behrens C., Pallottini A., Ferrara A., Gallerani S., Vallini L., 2018, MNRAS, 477, 552
Béthermin M., et al., 2015, A&A, 573, A113
Boselli A., et al., 2010, PASP, 122, 261
Bouwens R., et al., 2016, ApJ, 833, 72
Broekhoven-Fiene H., et al., 2018, ApJ, 852, 73
Calzetti D., Kinney A. L., Storchi-Bergmann T., 1994, ApJ, 429, 582
Calzetti D., Meurer G. R., Bohlin R. C., Garnett D. R., Kinney A. L., Leitherer C., Storchi-Bergmann T., 1997, AJ, 114, 1834
Calzetti D., Armus L., Bohlin R. C., Kinney A. L., Koornneef J., Storchi?Bergmann T., 2000, ApJ, 533, 682
Camps P., Trayford J. W., Baes M., Theuns T., Schaller M., Schaye J., 2016, MNRAS, 462, 1057
Capak P. L., et al., 2011, Nature, 470, 233
Capak P. L., et al., 2015, Nature, 522, 455
Carniani S., et al., 2015, A&A, 584, A78
Casey C. M., 2012, MNRAS, 425, 3094
Casey C. M., Narayanan D., Cooray A., 2014, Physics Reports, 541, 45
Casey C. M., et al., 2018a, ApJ, 862, 77
Casey C. M., Hodge J., Zavala J. A., Spilker J., da Cunha E., Staguhn J., Finkelstein S. L., Drew P., 2018b, ApJ, 862, 78
Cazaux S., Tielens A. G. G. M., 2002, ApJ, 575, L29
Chen C.-C., Cowie L. L., Barger A. J., Wang W.-H., Williams J. P., 2014, ApJ, 789, 12
Crocker R. M., Krumholz M. R., Thompson T. A., Clutterbuck J., 2018, MNRAS
Daddi E., Dannerbauer H., Krips M., Walter F., Dickinson M., Elbaz D., Morrison G. E., 2009, ApJ, 695, L176
Dale D. A., Helou G., 2002, ApJ, 576, 159
De Looze I., et al., 2014, A&A, 571, A69
Draine B. T., et al., 2007, ApJ, 663, 866
Dunlop J. S., et al., 2016, MNRAS, 466, 861
Dunne L., Eales S., Edmunds M., Ivison R., Alexander P., Clements D. L., 2000, MNRAS, 315, 115
Dwek E., 1998, ApJ, 501, 643
Eales S., et al., 2010, PASP, 122, 499
Egami E., et al., 2018, PASA, 35
Elbaz D., et al., 2011, A&A, 533, A119
Fazio G. G., et al., 2004, ApJ Supplement Series, 154, 10
Feldmann R., 2017, MNRAS: Letters, 470, L59
Feldmann R., Hopkins P. F., Quataert E., Faucher-Giguère C.-A., Kereš D., 2016, MNRAS, 458, L14
Feldmann R., Quataert E., Hopkins P. F., Faucher-Giguère C.-A., Kereš D., 2017, MNRAS, 470, 1050
Franco M., et al., 2018a, preprint, (arXiv:1803.00157)
Franco M., et al., 2018b, A&A, 620, A152
Fujimoto S., Ouchi M., Ono Y., Shibuya T., Ishigaki M., Nagai H., Momose R., 2016, ApJs, 222, 1
Galliano F., et al., 2011, A&A, 536, A88
Geach J. E., et al., 2013, MNRAS, 432, 53
Geach J. E., et al., 2017, MNRAS, 465, 1789
Gill S. P. D., Knebe A., Gibson B. K., 2004, MNRAS, 351, 399
Gonzalez-Alfonso E., Smith H. A., Fischer J., Cernicharo J., 2004, ApJ, 613, 247
Gould R. J., Salpeter E. E., 1963, ApJ, 138, 393
Griffin M. J., et al., 2010, A&A, 518, L3
Grogin N. A., et al., 2011, ApJ Supplement Series, 197, 35
Groves B., Dopita M. A., Sutherland R. S., Kewley L. J., Fischera J., Leitherer C., Brandl B., van Breugel W., 2008, ApJ Supplement Series, 176, 438
Gruppioni C., et al., 2013, MNRAS, 432, 23
Hahn O., Abel T., 2011, MNRAS, 415, 2101
Harrington K. C., et al., 2017, MNRAS, 474, 3866
Harvey P. M., et al., 2013, ApJ, 764, 133
Hashimoto T., et al., 2018, arXiv e-prints,
Hatsukade B., Ohta K., Seko A., Yabe K., Akiyama M., 2013, ApJL, 769, L27
Hatsukade B., et al., 2016, PASJ, 68, 36
Hayward C. C., Smith D. J. B., 2015, MNRAS, 446, 1512
Hayward C. C., Kereš D., Jonsson P., Narayanan D., Cox T. J., Hernquist L., 2011, ApJ, 743, 159
Hayward C. C., Jonsson P., Kereš D., Magnelli B., Hernquist L., Cox T. J., 2012, MNRAS, 424, 951
Hildebrand R. H., 1983, QJRAS, 24, 267
Hinshaw G., et al., 2013, ApJ Supplement Series, 208, 19
Hirashita H., Nozawa T., Villaume A., Srinivasan S., 2015, MNRAS, 454, 1620
Hodge J. A., et al., 2013, ApJ, 768, 91
Holland W. S., et al., 1999, MNRAS, 303, 659
Holland W. S., et al., 2013, MNRAS, 430, 2513
Hopkins P. F., 2012, MNRAS, 428, 2840
Hopkins P. F., 2015, MNRAS, 450, 53
Hopkins P. F., Quataert E., Murray N., 2012, MNRAS, 421, 3522
Hopkins P. F., Kereš D., Oñorbe J., Faucher-Giguère C.-A., Quataert E., Murray N., Bullock J. S., 2014, MNRAS, 445, 581
Hwang H. S., et al., 2010, MNRAS, 409, 75
Jonsson P., Groves B. A., Cox T. J., 2010, MNRAS, 403, 17
Kessler M. F., et al., 1996, A&A, 315, L27
Kewley L. J., Dopita M. A., 2002, ApJ Supplement Series, 142, 35
Kewley L. J., Ellison S. L., 2008, ApJ, 681, 1183
Kinney A. L., Bohlin R. C., Calzetti D., Panagia N., Wyse R. F. G., 1993, ApJ Supplement Series, 86, 5
Kirkpatrick A., et al., 2012, ApJ, 759, 139
Kirkpatrick A., et al., 2017, ApJ, 843, 71
Knollmann S. R., Knebe A., 2009, ApJ Supplement Series, 182, 608
Knudsen K. K., Watson D., Frayer D., Christensen L., Gallazzi A., Michałowski M. J., Richard J., Zavala J., 2016, MNRAS, 466, 138
Koekemoer A. M., et al., 2011, ApJ Supplement Series, 197, 36
Koyama Y., et al., 2015, MNRAS, 453, 879
Kriek M., Conroy C., 2013, ApJ, 775, L16
Lagache G., Abergel A., Boulanger F., Puget J.-L., 1998, A&A, 333, 709
Laporte N., et al., 2017, ApJ, 837, L21
Lee N., et al., 2013, ApJ, 778, 131
Leroy A. K., et al., 2011, ApJ, 737, 12
Liang L., Feldmann R., Faucher-Giguère C.-A., Kereš D., Hopkins P. F., Hayward C. C., Quataert E., Scoville N. Z., 2018, MNRAS: Letters, 478, L83
Lombardi M., Bouy H., Alves J., Lada C. J., 2014, A&A, 566, A45
Lutz D., 2014, ARA&A, 52, 373
Lutz D., et al., 2011, A&A, 532, A90
Ma X., Hopkins P. F., Faucher-Giguère C.-A., Zolman N., Muratov A. L., Kereš D., Quataert E., 2015, MNRAS, 456, 2140
Madau P., Dickinson M., 2014, ARA&A, 52, 415
Magdis G. E., et al., 2010, MNRAS, 409, 22
Magdis G. E., et al., 2012, ApJ, 760, 6
Magdis G. E., et al., 2013, A&A, 558, A136
Magnelli B., et al., 2012, A&A, 539, A155
Magnelli B., et al., 2013, A&A, 553, A132
Magnelli B., et al., 2014, A&A, 561, A86
Maiolino R., et al., 2008, A&A, 488, 463
Mannucci F., Cresci G., Maiolino R., Marconi A., Gnerucci A., 2010, MNRAS, 408, 2115
Murray N., Quataert E., Thompson T. A., 2005, ApJ, 618, 569
Murray N., Ménard B., Thompson T. A., 2011, ApJ, 735, 66
Narayanan D., Hayward C. C., Cox T. J., Hernquist L., Jonsson P., Younger J. D., Groves B., 2010, MNRAS, 401, 1613
Narayanan D., et al., 2015, Nature, 525, 496
Narayanan D., Davé R., Johnson B. D., Thompson R., Conroy C., Geach J., 2017, MNRAS, 474, 1718
Narayanan D., Conroy C., Davé R., Johnson B. D., Popping G., 2018, ApJ, 869, 70
Nguyen H. T., et al., 2010, A&A, 518, L5
Nordon R., et al., 2012, ApJ, 745, 182
Oliver S. J., et al., 2012, MNRAS, 424, 1614
Ono Y., Ouchi M., Kurono Y., Momose R., 2014, ApJ, 795, 5
Pilbratt G. L., et al., 2010, A&A, 518, L1

Poglitsch A., et al., 2010, A&A, 518, L2
Price S. H., et al., 2014, ApJ, 788, 86
Privon G. C., Narayanan D., Davé R., 2018, ApJ, 867, 102
Riechers D. A., et al., 2010, ApJ, 720, L131
Rigopoulou D., Pereira-Santaella M., Magdis G. E., Cooray A., Farrah D., Marques-Chaves R., Perez-Fournon I., Riechers D., 2017, MNRAS, 473, 20
Riguccini L., et al., 2015, MNRAS, 452, 470
Safarzadeh M., Hayward C. C., Ferguson H. C., Somerville R. S., 2016, ApJ, 818, 62
Schreiber C., Elbaz D., Pannella M., Ciesla L., Wang T., Franco M., 2018, A&A, 609, A30
Scoville N. Z., 2013, Evolution of star formation and gas. p. 491
Scoville N., et al., 2014, ApJ, 783, 84
Scoville N., et al., 2016, ApJ, 820, 83
Scoville N., et al., 2017, ApJ, 837, 150
Smail I., Ivison R. J., Blain A. W., 1997, ApJ, 490, L5
Sobral D., Smail I., Best P. N., Geach J. E., Matsuda Y., Stott J. P., Cirasuolo M., Kurk J., 2013, MNRAS, 428, 1128
Spinoglio L., et al., 2017, PASA, 34
Steidel C. C., et al., 2014, ApJ, 795, 165
Symeonidis M., et al., 2013, MNRAS, 431, 2317
Thompson T. A., Fabian A. C., Quataert E., Murray N., 2015, MNRAS, 449, 147
Thomson A. P., et al., 2017, ApJ, 838, 119
Trayford J. W., et al., 2017, MNRAS, 470, 771
Tremonti C. A., et al., 2004, ApJ, 613, 898
Tuffs R. J., Popescu C. C., Völk H. J., Kylafis N. D., Dopita M. A., 2004, A&A, 419, 821
Umehata H., et al., 2015, ApJ, 815, L8
Walcher J., Groves B., Budavári T., Dale D., 2010, Astrophysics and Space Science, 331, 1
Walter F., et al., 2012, Nature, 486, 233
Walter F., et al., 2016, ApJ, 833, 67
Watson D., Christensen L., Knudsen K. K., Richard J., Gallazzi A., Michałowski M. J., 2015, Nature, 519, 327
Weingartner J. C., Draine B. T., 2001, ApJ, 548, 296
Wild V., Charlot S., Brinchmann J., Heckman T., Vince O., Pacifici C., Chevallard J., 2011, MNRAS, 417, 1760
Wilson G. W., et al., 2008, MNRAS, 386, 807
Zahid H. J., Kewley L. J., Bresolin F., 2011, ApJ, 730, 137
Zavala J. A., et al., 2018a, MNRAS, 475, 5585
Zavala J. A., Casey C. M., Cunha E. d., Spilker J., Staguhn J., Hodge J., Drew P. M., 2018b, ApJ, 869, 71
Zhang D., Thompson T. A., 2012, MNRAS, 424, 1170
da Cunha E., et al., 2013, ApJ, 766, 13

This paper has been typeset from a TEX/LATEX file prepared by the author.